universität wien

DIPLOMARBEIT

Titel der Diplomarbeit

Isobar separation with post-stripping for the measurement of cosmogenic ^{10}Be at VERA

angestrebter akademischer Grad

Magister der Naturwissenschaften (Mag. rer.nat.)

Verfasser:	Leonard Michlmayr
Matrikel-Nummer:	9600539
Studienrichtung:	411 Physik (Stzw)
Betreuer:	O. Univ.-Prof. Dr. Walter Kutschera

Wien, am 27. August 2007

Abstract

^{10}Be ($t_{1/2} = 1.5\,\mathrm{Ma}$) is an important cosmogenic radionuclide in accelerator mass spectrometry (AMS). The biggest challenge in ^{10}Be measurement is the background of the stable abundant isobar ^{10}B. The two isobars cannot be separated efficiently by their small mass difference ($\Delta M/M = 6 \cdot 10^{-5}$). Their separation is based on the difference in energy loss of the ion beam in matter due to the different atomic number of ^{10}Be and ^{10}B respectively.

In the past at VERA, the Vienna Environmental Research Accelerator, an absorber in front of a particle detector was used to suppress the boron background.

An alternative approach to separate ^{10}Be and ^{10}B is post-stripping: after acceleration in the tandem accelerator to $\sim 8\,\mathrm{MeV}$, the ion beam passes through a $\sim 500\,\mathrm{nm}$ thick foil, which results in different residual energies of the isobars. The ions can be separated by an energy-sensitive analyzer.

I have implemented post-stripping for the measurement of ^{10}Be at VERA. In my measurement setup I have used silicon nitride foils for the stripping and a switching magnet as analyzer. Further, I took advantage of a new ΔE-E ionization chamber with a segmented anode.

Before I decided to use the switching magnet, I had considered alternative setups. Computer simulations of the ion optics helped finding a good setup.

Finally, post-stripping is used at VERA for the measurement of ^{10}Be. It has a lower measurement background ($^{10}\mathrm{Be}/^{9}\mathrm{Be} \sim 2 \cdot 10^{-15}$) than the method used before and the efficiencies of both methods are comparable.

Zusammenfassung

^{10}Be ($t_{1/2} = 1.5\,\mathrm{Ma}$) ist ein wichtiges kosmogenes Radionuklid für die Beschleuniger-Massenspektrometrie (AMS). Die größte Herausforderung bei der Messung von ^{10}Be ist der Hintergrund durch das stabile Isobar ^{10}B. Die beiden Isobare können nicht effizient anhand ihres kleinen Massenunterschieds ($\Delta M/M = 6 \cdot 10^{-5}$) getrennt werden. Die Trennung beruht auf dem unterschiedlichen Energieverlust des Ionenstrahls in Materie, aufgrund der verschiedenen Kernladungszahl von ^{10}Be und ^{10}B.

Früher wurde bei VERA, dem Vienna Environmental Research Accelerator, ein Absorber vor einem Teilchendetektor verwendet, um den Hintergrund durch Bor zu unterdrücken.

Ein alternativer Ansatz zur Trennung von ^{10}Be und ^{10}B ist Poststripping: nach der Beschleunigung im Tandem-Beschleuniger auf $\sim$8 MeV passiert der Ionenstrahl eine $\sim$500 nm dicke Folie. Die Isobare haben danach unterschiedliche Restenergien und können durch einen energieempfindlichen Analysator getrennt werden.

Ich führte Poststripping für die Messung von ^{10}Be bei VERA ein. Dabei verwendete ich Siliziumnitrid-Folien für das Strippen und einen Switcher-Magneten als Analysator. Außerdem nützte ich eine neue ΔE-E-Ionisationskammer mit einer unterteilten Anode.

Bevor ich mich für den Switcher-Magneten entschied, zog ich auch andere Messaufbauten in Erwägung. Computersimulationen halfen mir einen guten Messaufbau zu planen.

Schließlich wurde Poststripping bei VERA zur Messung von ^{10}Be verwendet. Poststripping hat einen niedrigeren Hintergrund (^{10}Be/^{9}B $\approx 2 \cdot 10^{-15}$) als die Absorbermethode bei vergleichbarer Effizienz.

Contents

List of Tables

List of Figures

1 Introduction

Accelerator mass spectrometry (AMS) is a refined isotope measurement technique with a wide range of applications. AMS allows the measurement of trace isotopes with an extremely high level of selectivity as well as sensitivity.

1.1 Background: AMS with ^{10}Be

Today AMS with ^{10}Be is routine at many AMS laboratories including VERA, the Vienna Environmental Research Accelerator. ^{10}Be is a cosmogenic radionuclide with a half-life of $1.5 \cdot 10^6$ a.

^{10}Be is produced via spallation induced by cosmic-ray particles in the atmosphere and by secondary particles in the upper layers of minerals in the earth's crust. The main spallation targets for the formation of ^{10}Be are nitrogen and oxygen. Spallation reactions have high threshold energies up to $\sim 200\,\mathrm{MeV}$. A large fraction of the cosmic rays are protons with energies in this range. [Lal and Peters, 1967]

Monaghan et al. [1985/86] estimate the global average production at $(1.21 \pm 0.26) \cdot 10^6 \mathrm{cm}^{-2}\mathrm{a}^{-1}$. The global inventory of ^{10}Be is determined by the balance of production and radioactive decay. With the average production rate cited above, the global inventory is about $2 \cdot 10^5$ kg.

1.1.1 Applications

^{10}Be has a wide range of applications. Many of the applications can be improved by using ^{10}Be in combination with other cosmogenic radionuclides, for example ^{26}Al. My thesis is not concerned with applications, but I will briefly present some examples of applications.

Applications in geoscience

The production rate of ^{10}Be in stones depends on the level of exposure to cosmic rays. The intensity of cosmic rays in the earth's crust rapidly decreases with depth because of absorption and nuclear reactions. Therefore the production of ^{10}Be is mostly limited to the surface layers.

An important application of this is *exposure dating*, i.e. determining the duration of exposure of surfaces that were covered in the past. If we know the local irradiation—which depends on the latitude and the inclination of the surface for example—and the chemical composition of the stone, we can estimate the production rate of ^{10}Be. Therefore we can estimate the time of exposure from the current content of ^{10}Be.

A complementary application to exposure dating is *burial dating*. A surface that had been exposed to cosmic rays may have been buried later. In the ideal case, the production of cosmogenic radionuclides stops after the burial and the content decreases by radioactive decay. There are two unknown parameters: the time of exposure prior to the burial and the time of burial. Therefore "burial dating requires at least two nuclides" [Granger and Muzikar, 2001].

The irradiation by charged particle cosmic rays is modulated by the geomagnetic field. Therefore the production rate of ^{10}Be is modulated by the geomagnetic field, too. ^{10}Be in aeolian loess sediments can be used for the *retrospection of the geomagnetic field,* provided that there is information on the precipitation rate [Zhou et al., 2007].

Applications in climate research

Glacial ice can shield a rock surface from cosmic rays, too. Therefore burial dating and exposure dating allow the *dating of glaciation and deglaciation* [Ivy Ochs, 1996].

Also, glaciers are important climate archives. The ratio of the production rates of ^{10}Be and ^{26}Al is believed to be constant with time. Therefore ^{10}Be and ^{26}Al can potentially provide absolute dating of very deep ice cores. Matthias Auer has been working on this at VERA [Auer, expected 2007; Auer et al., 2007].

The atmospheric production of ^{10}Be and ^{7}Be ($t_{1/2} = 53\,\mathrm{d}$) can be used as tracer isotopes for the stratosphere-to-troposphere transport. VERA took part in this research in the framework of the STACCATO project [Priller et al., 2004].

1.1.2 Measurement

^{10}Be decays via beta-minus decay to the ground state of ^{10}B with a half-life of $1.5{\cdot}10^6$ a. Because of the long half-life, traces of ^{10}Be cannot be measured by detection of its decay products. It has to be measured by AMS rather than beta counting. For example, to achieve a statistical uncertainty of 5%, at least 400 events have to be counted. If we consider a sample of 1 mg BeO with a ^{10}Be/^{9}Be ratio of 10^{-12}, it will contain $2.4 \cdot 10^7$ atoms of ^{10}Be. With beta counting we would have to wait about 37 years for 400 atoms to decay. With AMS the ^{10}Be atoms can be counted directly. Under usual conditions we have a BeO^- current of 2 µA and an efficiency[1] of 4%. Thus 400 ^{10}Be ions can be counted within 14 minutes (neglecting time needed for sample preparation).

Typically, in various applications the number of ^{10}Be nuclei per mass of sample material is of interest. However, in AMS we measure isotope ratios rather than the absolute amount. We measure the count rate of the trace isotope and the current of the abundant isotope. Therefore a controlled amount of ^{9}Be is added to the sample in the sample-preparation process. The AMS measurement delivers the isotope ratio of ^{10}Be and ^{9}Be, ^{10}Be/^{9}Be. The typical isotope ratios of ^{10}Be/^{9}Be in AMS are in the range of 10^{-14} to 10^{-10}.

The main problem in ^{10}Be measurement is the suppression of the abundant stable isobar ^{10}B. Although boron can be reduced in chemical sample preparation, there are still high ratios of ^{10}B/^{9}Be in the sample. For example, based on my measurements, for the S555 standard material (which is pure BeO, mixed with copper) I estimate a ^{10}B/^{9}Be ratio of roughly 10^{-6}, i.e. 1 ppm. If we choose BeO^- as negative ions, without a suppression of boron this high boron content would mean that the detector would have to register about 10^6 events per second, which is beyond its capabilities. Thus ^{10}B not only needs to be discriminated from ^{10}Be in the AMS measurement, but it also needs to be suppressed by several orders of magnitude before the final detector.

There are two methods to reduce and discriminate the high boron background in a ^{10}Be measurement that are well established in routine measurements at many AMS facilities: first, the use of an absorber in front of an energy sensitive detector and,

[1] In this case the efficiency is ^{10}Be atoms detected / ^{10}Be atoms in the beam

second, the use of post-stripping or double stripping in combination with an energy sensitive filter [Raisbeck et al., 1984]. The first of these methods is preferable for higher energy accelerators, while the second is more suitable for smaller machines and can be used with machines down to 0.6 MV terminal voltage, as recently demonstrated by Grajcar et al. [Grajcar, 2005; Grajcar et al., 2004].

Zhao et al. [2004] suggest the use of BeF^- instead of BeO^- on the injection side of the accelerator, which was implemented by Grajcar et al. [2007]. Therewith, boron can be suppressed, because BF^- is unstable, but the BeF^- current that can be achieved in an ion source like ours is substantially lower than the BeO^- current.

The absorber method has been used successfully at VERA—a 3 MV Pelletron—for many years now [Priller et al., 2000]. Since long there have been plans to establish the second approach with post-stripping, too.

The task for this thesis is to investigate the operability and expedience of ^{10}Be measurements with post-stripping at VERA and to evaluate its efficiency and quality in comparison to the established method.

First, I have done computer simulations of the ion optics for various possible experimental setups in order to choose an optimum setup for real experiments. Finally, after some experimental tests post-stripping has been successfully applied for ^{10}Be measurements at VERA.

1.2 Overview of VERA

The Vienna Environmental Research Accelerator is an AMS facility established in 1996. It has been designed to allow the acceleration and transport of ions from hydrogen up to the heaviest elements [Kutschera et al., 1997]. The primary mission of VERA is the tracing of long-lived radionuclides in our environment.

The isotope being measured the most is ^{14}C, the most important AMS isotope today. Other isotopes that have been successfully measured at VERA include: ^{10}Be, ^{26}Al, ^{36}Cl, ^{41}Ca, ^{55}Fe, ^{129}I, ^{182}Hf, ^{210}Pb, ^{236}U, ^{244}Pu [Steier et al., 2004, 2005]. I started my work in Summer 2005. The setup of VERA at that time is shown in figure 1.1.

VERA was delivered in 1995 [Kutschera et al., 1997] and had a major upgrade

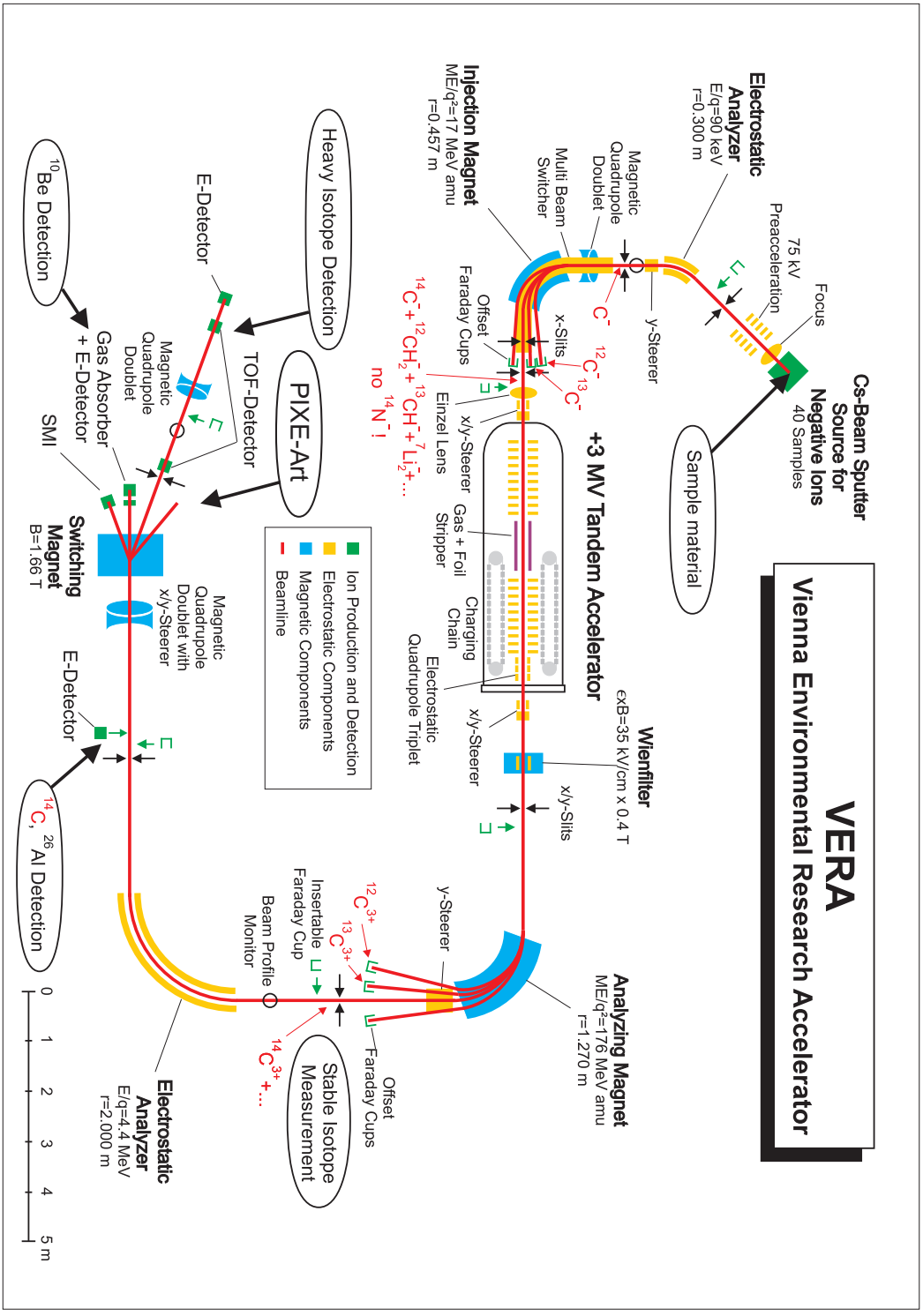

Figure 1.1: VERA in 2005. This figure is based on a figure by Vockenhuber [2004].

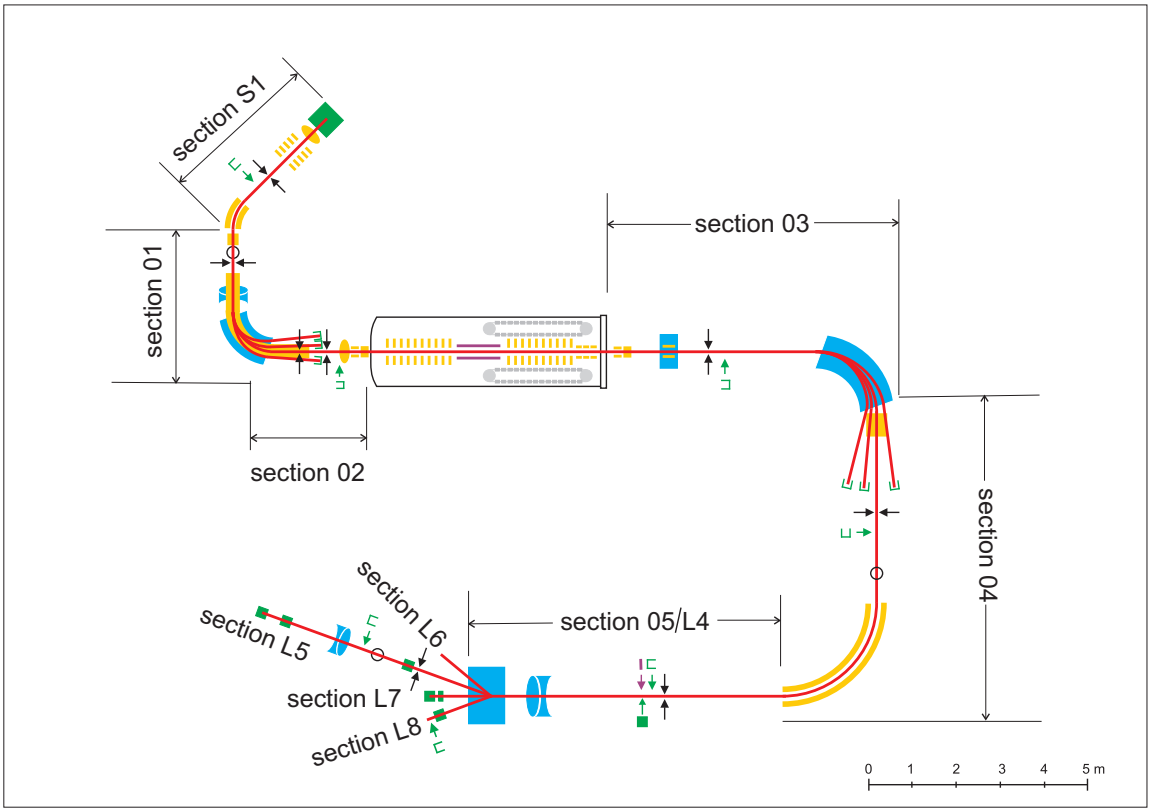

Figure 1.2: Names of the beam-line sections of VERA. This figure is based on a figure by Vockenhuber [2004].

in 2001, when an electrostatic analyzer (ESA) was added to the high-energy beam line [Priller et al., 2002; Vockenhuber, 2004].

In the following I will briefly describe VERA.

1.2.1 The negative ion source

A "SNICS" (Source of Negative Ions by Cesium Sputtering) ion source is used for the production of the negative ions. The source is at a potential of about -65 kV. The sample material is pressed into a target cathode. A sample wheel holds 40 target cathodes. The sample wheel is at a potential of about -5 kV relative to the source potential. Thus, the anions extracted from the source have an energy of about 70 keV. The ions are sputtered from the target cathode by a positively charged cesium sputter beam. Because the ions may retain a variable fraction of the energy from the cesium

beam, the ions' energy is not completely monoenergetic.

As VERA is a tandem accelerator, the ions emitted from the source have to be negative and the ion source can only emit negative ions. For some chemical elements—as is the case with beryllium—negative atomic ions can hardly be produced. Therefore we use beryllium oxide, the cathode material that is recommended by the Negative Ion Cookbook [Middleton, 1989], mixed with copper and inject $Be^{16}O^-$ into the tandem. (The copper is used in order to improve the electric and thermal conductivity.) We get a current of 1-5 µA of $^9Be^{16}O^-$ from the ion source.

1.2.2 The injector beam line

To remove the tails of higher or lower energy from the ion beam, the injector beam line contains a 45 ° electrostatic analyzer (ESA) with a radius of 0.3 m. It is an energy selective element. To be more precise, for a fixed voltage an electrostatic analyzer selects ions of a specific $\frac{E}{q}$, where E is the kinetic energy of the ion and q is its charge.

The next selective element is a 90 ° double-focusing magnet with a radius of 0.457 m. A magnetic field selects the ion's momentum mv, or more precisely ions of the same magnetic rigidity:

$$B\rho = \frac{mv}{q} = \sqrt{\frac{2Em}{q^2}} \tag{1.1}$$

(ρ is the radius of the path, B the magnetic field, q the electric charge of the ion) With the energy and charge already defined by the ESA, the ions that get injected to the accelerator after passing the magnet have the mass m. For a charge of $q = -e$ the maximum possible energy–mass product Em for the low energy bending magnet is 17 MeV · amu.

The magnet is equipped with a so-called multi-beam switcher (MBS) device: the magnet chamber is insulated and a bias voltage can be applied. The ions are accelerated at the entrance of this chamber and decelerated at its exit. Inside the chamber they gain energy depending on the voltage applied. The multi-beam switcher allows fast switching between different masses that will be injected: while the magnetic field is constant the ions' energy can be adjusted to allow a beam of different particle mass to be injected into the accelerator. Electrostatic elements can be changed much faster and in a more reproducible manner than magnetic elements. Actually the

beam switcher can switch between two masses within 20 µs. In normal measurement mode, the multi-beam switcher is set to up to four different voltages within a machine cycle, which is typically about 250 ms. Within each machine cycle we usually inject the stable isotope beam ($^{9}Be^{16}O^{-}$) into the accelerator once in order to measure the currents in an offset Faraday-cup on the high-energy side for about 300 µs, then measure the stable isotope current with an offset Faraday-cup at the low-energy side for about 300 µs, and finally inject the radioactive isotope beam ($^{10}Be^{16}O^{-}$) for the rest of the cycle to count the radioactive isotope ions ($^{10}Be^{n+}$) with a particle detector.

The injector beamline also contains a number of focusing and steering elements. With help of these elements the beam can be directed through the thin stripper canal in the accelerator terminal.

1.2.3 The Pelletron accelerator

The Pelletron is a 9SDH-2 tandem from National Electrostatics Corporation (NEC). It is specified for a maximum voltage of 3 MV, but when well conditioned it can be operated at voltages up to 3.6 MV [Steier et al., 2005].

The voltage is generated by a Van-de-Graaff generator. Instead of a belt it uses two Pelletron chains for the charge transport to the terminal. The generator and the accelerator beamline are inside a pressure tank which is filled with SF_6 of about 6 bar.

The negative ions are accelerated on their way in direction to accelerator terminal, which has a positive electric potential. At the terminal the ions have an energy of $E_0 + U_T q$, where E_0 is the injection energy, U_T is the terminal voltage, and q is the charge of the ion. The ions can be stripped off electrons with a stripping gas or a foil. For ^{10}Be measurements O_2 is used as a stripping gas, as is the case with most AMS measurements at VERA. In case of molecular ions, usually a Coulomb explosion follows the stripping process, which breaks up the molecules to monoatomic ions. If M is the mass of the injected ion and M_k the mass of the fragment k, then the energy of the fragment k leaving the stripper is given by

$$E_k^{\text{Terminal}} = \frac{M_k}{M} (E_0 + U_T q) \tag{1.2}$$

For a terminal voltage of 3.00 MV the energy of ^{10}Be injected as $^{10}Be^{16}O^-$ after the stripping process is 1.18 MeV. For ^{9}Be injected as $^9Be^{16}O^-$ it is 1.11 MeV.

Generally the ions do not all have the same charge state. The stripping yield for each charge state is a function of the area density of the stripping medium and the velocity of the ion. With growing area density (i.e. growing gas pressure or foil thickness) the stripping yield reaches an equilibrium. The equilibrium stripping yield is a function of the velocity of the ion. For example, with a terminal voltage of 3 MV about 55% of the ^{9}Be ions will be in charge state 2+ and only about 7% in charge state 3+. The stripper canal is 80 cm in length and the stripper gas pressure is measured to 1.3 Pa.

The positive ions from the terminal are accelerated again on the way to the high-energy side of the accelerator, now with a charge Q. The total energy of the ion k with the charge Q is

$$E_{\mathrm{kin}} = \frac{M_k}{M}\left(E_0 + U_{\mathrm{T}}q\right) + U_{\mathrm{T}}Q \tag{1.3}$$

Thanks to the change of the sign of the ions' charge, a tandem accelerator makes use of the same potential difference twice. Further, the analyzing beamlines are on ground potential and there is no need to have the ion source inside the accelerator tank, which is very convenient.

1.2.4 The high-energy analyzing beam line

The high-energy analyzing beam line consists of a 90° double-focusing magnet with 1.27 m radius and a 90° electrostatic analyzer (ESA 04) with 2.0 m radius. Similar to the injector beam line, the electric and magnetic elements provide a filter for specific $\frac{\sqrt{2ME}}{Q}$ and $\frac{E}{Q}$. The maximum magnetic rigidity of ions that the analyzer magnet can bend is 1.9 Tm. The maximum $\frac{E}{Q}$ for ions that the ESA can bend is 4.4 MV.

In the beamline section following the ESA 04 there is a Si-detector, which can be inserted to the beam line. It is used for radiocarbon measurements, however, it is not used in ^{10}Be measurements.

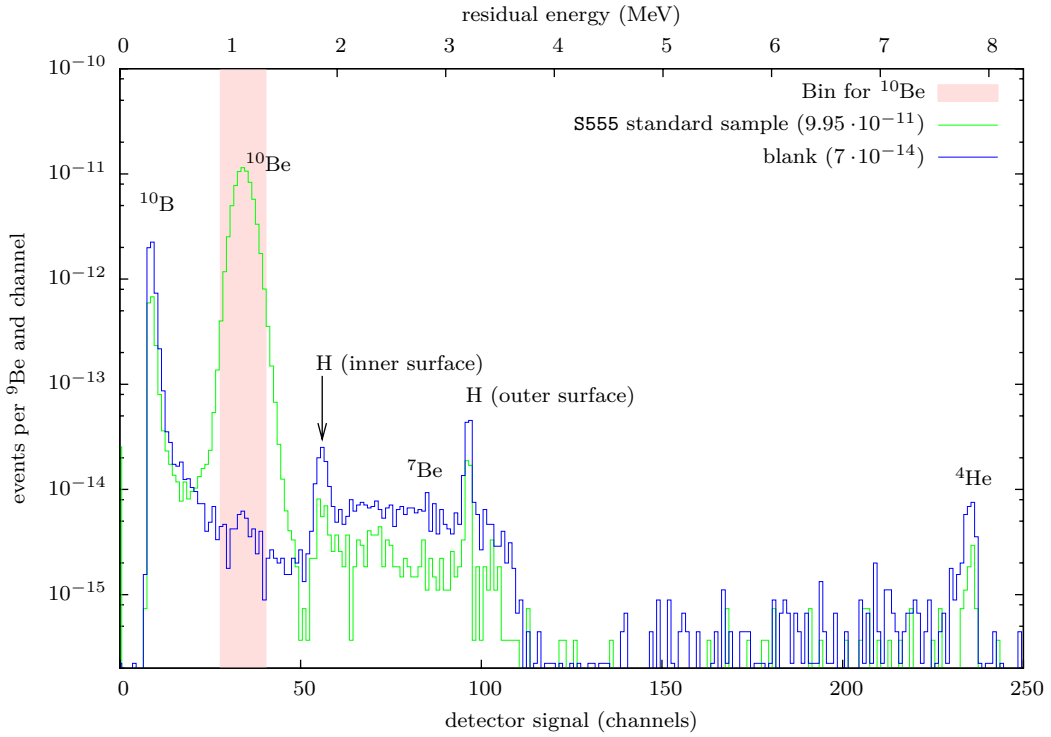

Figure 1.3: ^{10}Be measurement spectra of the absorber detector: plotted are the sum spectra of two different samples. The ordinate shows the events per channel divided by $t\frac{I}{3e}$, where t is the measurement time, I is the average $^{9}Be^{3+}$ current, and e is the elementary charge. S555 is a standard material known to have a ^{10}Be/^{9}Be ratio of $(9.95 \pm 0.03) \cdot 10^{-11}$. The blank material shows the background of $(7 \pm 2) \cdot 10^{-14}$. The spectra exhibits ^{10}B, ^{10}Be, ^{1}H from elastic scattering, and ^{7}Be and ^{4}He from a nuclear reaction (see text).

1.2.5 The switching magnet

The switching magnet is a bending magnet with exit ports at the angles $-20°$, $0°$, $20°$, and $40°$ nominally. The ion beam can be guided to each port by setting an appropriate magnetic field for the switcher magnet. The geometry of the switcher-magnet will be discussed in more detail in section 2.4.5.

1.2.6 The absorber detector

The ^{10}Be detector used for the absorber consists of a titanium window of 1.3 mg/cm^2, a volume with 6 cm in length filled with CO_2 with a pressure of about 75 hPa and a surface barrier detector. The CO_2 pressure can be controlled and is adjusted such,

that most of the boron ions are stopped inside the gas volume, but most of the beryllium will enter the particle detector. There will still be some boron ions reaching the detector, but they can be discriminated by the different residual energy.

Figure 1.3 shows spectra acquired with that detector, when $^{10}Be^{3+}$ ions of 10.4 MeV are used from the tandem accelerator.

H ions reach the detector, because boron ions kick hydrogen atoms, adsorbed at the titanium entrance window, into the detector via elastic scattering. (There are two hydrogen peaks in the residual energy spectra because most of the hydrogen is located at the two surfaces of the entrance window. The energy of the boron ions is higher at the outer surface than at the inner surface of the entrance window.)

Because the energy loss of the ^{1}H ions is very low, I use the peak of ^{1}H from the outer surface for a rough calibration of the spectra. Scattering kinematics predicts the maximum energy of the ^{1}H ions of 3.4 MeV. With the help of SRIM [Ziegler and Biersack, 2003] I estimate an energy loss in the titanium foil and the absorber gas of about 0.2 MeV for ^{1}H.

At the inner surface the boron energy is reduced by about 4 MeV. Therefore hydrogen atoms from the inner surface of the window have about 2 MeV residual energy.

The spectra also shows ^{4}He and ^{7}Be which are products of the exothermic nuclear reaction ^{1}H(^{10}B, ^{7}Be)^{4}He ($Q = 1.145$ MeV). These products have wide ranges of energies. In this example, the energy of ^{7}Be ranges from 2.5 MeV to 11.1 MeV and the energy of ^{4}He ranges from 0.5 MeV to 9.1 MeV. The energy of a reaction product depends on the angle of the particle's momentum relative to the incident beam direction. Only for small angles, the particle can reach the detector, which lies in forward direction. These angles correspond to energies near the minimum and maximum values of the ranges. Assuming a maximum accepted angle of 0.1 rad, the width of energy range for the ^{4}He is 0.14 MeV and for ^{7}Be it is 0.31 MeV.

For this kinematic reason and for the different energy straggling in the absorber, the α peak in the spectrum is narrower than the ^{7}Be peak.

The residual energies of the α-particles is very high due to the low stopping power, thus α-particles can be separated easily. However, ^{7}Be might add to the background, because the stopping power and energy straggling are higher than for α-particles.

1.3 Motivation for the use of post-stripping

The absorber method only works for energies above about 1 MeV/amu. Therefore, the Be^{3+} charge state has to be selected at the high-energy side of the analyzing beam line. This charge state has a low yield of 7% using gas stripping in the accelerator terminal. Using foil stripping would increase the stripping yield—the program Q.xls[Doyle] suggests 27%—but also increase the effect of Coulomb explosion, reducing the beam quality.

Another consequence of the high energy needed is the possibility of the nuclear reaction $p(^{10}B, \alpha)^{7}Be$. There are protons at the surfaces of the titanium entrance window. The ^{7}Be from this nuclear reaction may add to the measurement background.

With post-stripping we hope to be able to use the Be^{2+} charge state. This removes both of the disadvantages described above. It may increase the efficiency and reduce the background.

2 Planing phase

Before starting with the experiments, I did calculations in order to find a measurement setup with a good prospect of success. The main question is, which of the available energy sensitive elements to use for the post-stripping method. The setup should suppress background sufficiently and maintain a good transmission for ^{10}Be.

2.1 Measurement background

The force acting on a charged particle moving through an electric and magnetic field is given by equation (2.1).

$$\vec{F} = q\left(\vec{\mathcal{E}} + \vec{v} \times \vec{B}\right), \tag{2.1}$$

where q is the charge, v the particles velocity, $\vec{\mathcal{E}}$ the electric field, and $\vec{B}$ the magnetic field.

The equation of motion for the particle in a static electric and magnetic field is therefore

$$m\ddot{\vec{x}} = q\left(\vec{\mathcal{E}} + \dot{\vec{x}} \times \vec{B}\right) \tag{2.2}$$

Particles of the same mass and same charge will always behave the same under the influence of electric and magnetic fields.

The main background for ^{10}Be mass spectrometry is the isobar ^{10}B. The mass difference is only $6 \cdot 10^{-4}$u. (Based on [Audi and Wapstra, 1995].)

2.1.1 A/Q ambiguities

In theory, isobars are not the only background that cannot be separated completely by electrostatic or magnetic elements. In the following consideration, we can generally

assume integer masses ($M = A \cdot amu$), because in AMS the mass resolution is far below that which is needed to separate isobars.

The electrostatic and magnetic elements are only sensitive to $\frac{M}{Q}$. To understand this, it is useful to look at the total energy that an ion has after the acceleration process.

In the following I will denote parameters of the ions on the low energy side of the accelerator with the index l and parameters of the ions at the high energy side with the index h.

Now I will demonstrate that any nuclide with the same mass over charge ratio $^{M_\mathrm{h}}/_{Q_\mathrm{h}}$ as the nuclide of interest cannot be separated by the high energy mass spectrometer if it has been injected to the accelerator. For example if we choose a charge of $Q_\mathrm{h} = +2e$ for the ^{10}Be at the high energy side, $^{25}\mathrm{Mg}^{5+}$ cannot be separated.

As Kilius et al. [1997] showed, the energy–charge ratio $^{E_\mathrm{h}}/_{Q_\mathrm{h}}$ on the high energy side—after the acceleration in the terminal—depends on $^{M_\mathrm{h}}/_{Q_\mathrm{h}}$ and $^{M_\mathrm{l}}/_{Q_\mathrm{l}}$ rather than M_h or M_l. This can simply be shown as follows:

For ions with the negative charge Q_l injected to the accelerator, the injection energy $Q_\mathrm{l}U_\mathrm{i}$ (U_i shall be the injector voltage) and the energy gained on the way to the terminal $Q_\mathrm{l}U_\mathrm{T}$ (with U_T being the terminal voltage) are independent of the mass M_i. The energy at the terminal is

$$E_\mathrm{T} = Q_\mathrm{l}(U_\mathrm{i} + U_\mathrm{T}) \tag{2.3}$$

When the molecule is broken up, a fragment with the mass M_h retains the energy fraction $\frac{M_\mathrm{h}}{M_\mathrm{l}}E_\mathrm{T}$. Each fragment then gains the additional energy $Q_\mathrm{h}U_\mathrm{T}$. The total energy is

$$E_\mathrm{h} = \frac{M_\mathrm{h}}{M_\mathrm{l}}E_\mathrm{T} + Q_\mathrm{h}U_\mathrm{T}, \text{ thus} \tag{2.4}$$

$$\frac{E_\mathrm{h}}{Q_\mathrm{h}} = \frac{M_\mathrm{h}}{Q_\mathrm{h}} \cdot \frac{Q_\mathrm{l}}{M_\mathrm{l}}\,(U_\mathrm{i} + U_\mathrm{T}) + U_\mathrm{T} \tag{2.5}$$

Ions with the same $^{M_h}/_{Q_h}$ will also have the same $^{E_h}/_{Q_h}$. This applies to our ^{10}Be measurement setup as follows: On the low energy side I inject $^{10}\mathrm{Be}^{16}\mathrm{O}^-$ with a mass of 26 u. $\frac{M_\mathrm{l}}{Q_\mathrm{l}} \approx 26\,^{u}/_{\mathrm{e}}$

On the high energy side we set the analyzing magnet and the ESA to accept $^{10}Be^{2+}$, thus an M_h/Q_h of $5\,u/e$.

According to the reasoning above, all ions with an M_h/Q_h of $5\,u/e$ can pass the high energy analyzer setup. In theory, this may be $^{10}B^{2+}$, $^{15}N^{3+}$, and $^{25}Mg^{5+}$ as well as $^{9}Be^{1}H^{2+}$, $^{14}N^{1}H^{3+}$, ... The noble gas ^{20}Ne cannot be injected since if cannot form a compound with mass 26 u.

The only background species identified in the experiments of this work are ^{10}B and ^{9}BeH.

possibly injected as	high energy ion	
$^{9}Be^{16}O^{1}H^{-}$	$^{9}Be^{1}H^{2+}$	detected
$^{10}B^{16}O^{-}$	$^{10}B^{2+}$	detected
$^{15}N^{11}B^{-}$	$^{15}N^{3+}$	not observed
$^{25}Mg^{1}H^{-}$	$^{25}Mg^{5+}$	not observed

Table 2.1: Possible background ions due to A/q ambiguities. Note: some of the listed background ions may or may not exist up to the post-stripping foil but do not reach the detector. We have made no effort to detect and identify these species.

2.1.2 ^{10}B

Boron is an ubiquitous element. It has two stable isotopes ^{10}B (20%) and ^{11}B (80%). It is always present in beryllium sample material. Well prepared ^{10}Be samples still contain ^{10}B in the order of 10^{-6} per ^{9}Be, which is 4 to 9 orders of magnitude above the range of typical $^{10}Be/^{9}Be$ measurements.[1] The mass difference is too small to allow a separation by electrostatic or magnetic elements in AMS.

^{10}B is the main interference. The ionization chamber can discriminate ^{10}B and ^{10}Be by their different stopping power with a selectivity of at least $3 \cdot 10^{6}$, but this is not enough for all applications. Further, without a suppression of boron the intensity of the beam would be too high for the detector and the signal processing to cope with.

[1] As I will explain in section 3.4.3 VERA is intermediately tuned for ^{10}B. From the detector count-rate and the $^{9}Be^{2+}$ current I can estimate the $^{10}B/^{9}Be$ ratio. There are two major uncertainties: I have to use an attenuator when counting boron and the ionization yield and the stripping yields for beryllium and boron are different in general. For the standard material `S555` I estimate the ratio at $(7 \pm 2) \cdot 10^{-7}$, without a correction for the ionization efficiencies and stripping yields.

2.1.3 $(^9Be^{16}OH)^-$ injected and stripped to $(^9BeH)^{2+}$

At the high energy side of the accelerator we select the doubly-positive ion $^{10}Be^{2+}$. For this charge state there is also molecular background. Theory predicts that the dication $(BeH)^{2+}$ is stable in its ground state and the first five excited vibrational levels have lifetimes greater than 1 µs [Nicolaides et al., 1990]. Experimental observations of $(BeH)^{2+}$ were reported by e. g. Franzreb et al. [2005] with secondary ion mass spectrometry and Grajcar [2005] with a 0.6 MV tandem accelerator.

Thus, we have to consider $(BeH)^{2+}$ background up to the post-stripping foil. After the post-stripping foil we select the charge state 3+ or 4+. For these charge states no molecular background is to be expected. The analyzing element will separate ^{9}Be having less energy than ^{10}Be. However, some $^9Be^{3+}$ respectively $^9Be^{4+}$ can reach the detector via scattering at the residual gas. We have identified such background in the detector as will be explained in section 3.2.4.

If a $(BeH)^{2+}$ molecular ion can survive the stripping process in the accelerator, it will have about the same energy as ^{10}Be before it reaches the post-stripping foil. When a $(BeH)^{2+}$ is broken up in the post-stripping foil, the $^9Be^{n+}$ ion has $\frac{9}{10}$ of the molecule ion's energy. Therefore the ^{9}Be can be discriminated in the detector by its lower energy. The spectrum in figure 3.10 on page 48 shows a long tail of scattered ^{9}Be ions. The maximum energy of the ^{9}Be is about 10 % below the energy of ^{10}Be.

2.2 The concept of post-stripping

In order to suppress ^{10}B we have to make use of processes that depend not only on the ion's mass, but also on the ion's atomic number.

As will be discussed in section 2.3, the effects of the passage of fast ions through matter depend on the atomic number. The stopping power is roughly proportional to Z^2. Therefore, by the passage through a thin foil the $^{10}_5$B will lose more energy than $^{10}_4$Be.

The different energies of the ions after passing a thin foil can be used to suppress the ^{10}B with an (energy sensitive) analyzing electric or magnetic element.

Also the charge distribution after the passage through the foil will depend on the atomic number. This effect is not crucial for the suppression of ^{10}B in our ^{10}Be

measurements. However, the charge state after post-stripping can be higher than before. This is important as it allows getting rid of molecular background, i.e. $^{9}\mathrm{BeH}^{2+}$ as discussed above.

This method of suppressing ^{10}B background by the passage of the beam through a foil has been applied by Raisbeck et al. [1984] first and it is usually referred to as post-stripping, double stripping, or degrading method.

2.3 Passage of heavy ions through thin foils

2.3.1 Energy loss

The passage of heavy ions through thin foils involves a number of interactions: ion–electron collisions, ion–nucleus collisions, electron uptake and loss, and—for high energies—nuclear reactions. Besides excitation or ionization of the projectiles, the interactions involve a transfer of the ions' kinetic energy to the target material, e.g. by transfer of momentum to target atoms and excitation or ionization of target atoms.

Without going into detail about the interactions, we can describe the mean energy loss by the *stopping power* ϵ which is defined by

$$\epsilon = -\lim_{N\Delta x \to 0} \frac{\langle \Delta E \rangle}{N\Delta x} \tag{2.6}$$

where $N\Delta x$ denotes the area density of the target and $\langle \Delta E \rangle$ is the energy loss of the ion.

There exist a number of models for the prediction of ϵ. An overview of these is given by Golser [1995]. The Bethe–Bloch equation (2.7) is a widely used model for the high velocity regime above $10v_0$ corresponding to 25 MeV for a mass of 10 u.[2] This is above the regime of my measurements which are in the range of 6 MeV to 8 MeV. Nevertheless, I will use the Bethe–Bloch model first to discuss the general features of the stopping power.

[2] $v_0 = \alpha c = {}^{e^2}/_{4\pi\epsilon_0\hbar}$, the Bohr velocity

In the Bethe–Bloch model the stopping power is given by the Bethe–Bloch equation:

$$\epsilon = -\frac{\mathrm{d}E}{N\mathrm{d}x} = \frac{4\pi Z_1^2 e^4}{m_\mathrm{e} v_1^2 \left(4\pi\epsilon_0\right)^2} Z_2 \left\{ \ln\frac{2m_\mathrm{e}v_1^2}{I} + \ln\frac{1}{1-\beta^2} - \beta^2 - \frac{C}{Z_2} - \frac{\delta}{2} \right\} \tag{2.7}$$

(Z_1,Z_2... the atomic number of the projectile (1) and the target (2); v_1... the projectile's velocity; $\beta = {}^{v_1}/_{c}$; I, C, δ... parameters generally extracted from measurements.)

The stopping power ϵ is proportional to Z_1^2 which is the most important feature for the application described in this thesis. From this we can expect that the stopping power for ^{10}B would be about 50 % above the stopping power for ^{10}Be.

For energies below the Bethe–Bloch regime, the projectile will not be fully stripped. The Bethe–Bloch model can be extended to some degree by replacing Z_1 with an effective charge Z_1^*. In general $0 \leq Z_1^* \leq Z_1$. For low energies Z_1^* will drop and electrons will shield the nucleus, making the stopping power less dependent on the atomic number.

2.3.2 Energy straggling and angular straggling

The energy loss and scattering of ions in matter is a statistical process. Therefore, the energies and scattering angles of the ions behind a foil will be statistically distributed, thus there will be energy straggling and angular straggling.

For thin foils, the number of interactions is approximately proportional to the thickness of the foil. Thus, the standard deviation of the energy and the straggling angle can be estimated to be proportional to the square root of the area density.

2.3.3 Separation

For any analyzer, a high energy resolution will help suppressing the boron background, but it will also suppress some of the beryllium, because of energy straggling. Therefore, a high difference of the energies of the two isobars, a high ΔE, is preferable as it allows the use of an analyzer with a lower resolution.

In a wide range, ΔE grows with the thickness of the foil. On the other hand, the energy straggling increases. Therefore the ΔE alone is not a good measure for the separation. The energy straggling has to be included too.

In [Steier et al., 2005] the separation is defined as in equation (2.8), where E_{A} and σ_{A} are the residual energy and its standard deviation of the ion species A respectively. E_{B} and σ_{B} are the same for the ion species B.

$$S_{\mathrm{A,B}} = \frac{|E_{\mathrm{A}} - E_{\mathrm{B}}|}{\sqrt{\frac{1}{2}\left(\sigma_{\mathrm{A}}^2 + \sigma_{\mathrm{B}}^2\right)}} \tag{2.8}$$

Figure 2.1 shows the separation.

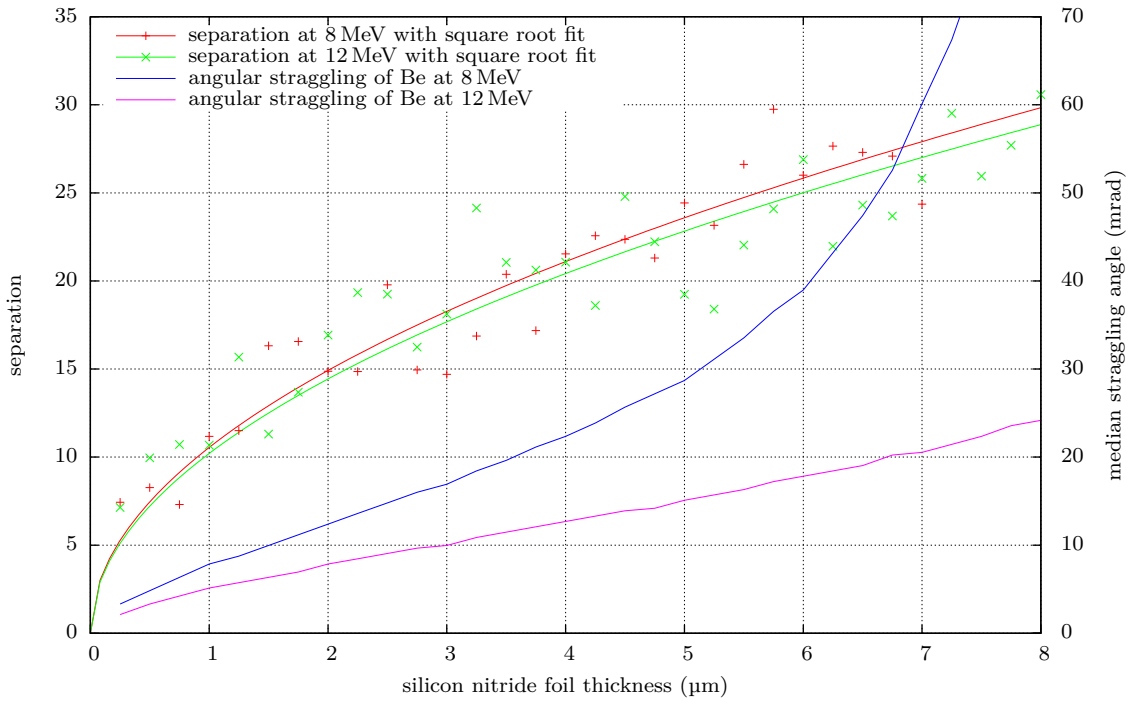

Figure 2.1: This plot shows the separation as defined in (2.8) and the median of the straggling angle of ^{10}Be vs. the foil thickness. The fit lines for the separation are just a guide to the eye, no model has been applied. The data are from TRIM [Ziegler and Biersack, 2003] simulations.

2.3.4 Equilibrium charge state distribution

Ions passing through a foil exchange electrons with the foil material. The statistical distribution of charge states of the ion beam will by and by change from the initial charge state distribution to an equilibrium charge state distribution. If the foil is just

thick enough for equilibrium to be reached, the charge state distribution does not depend directly on the foil thickness.

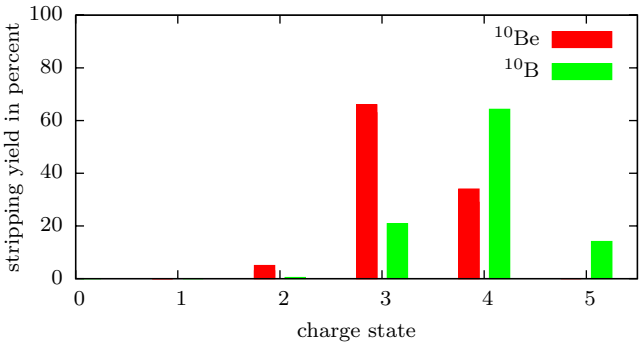

Figure 2.2: The charge state distribution suggested by `Q.xls` [Doyle] for a ^{10}Be beam and a ^{10}B beam after passing a carbon foil with 7 MeV. The mean charge state is 3.3 for beryllium and 3.9 for boron.

Semi-empirical formulas for the prediction of the equilibrium charge state distribution have been published by Sayer [1977] and can be calculated by the convenient spreadsheet `Q.xls` by [Doyle]. Figure 2.2 shows the output of `Q.xls` for ^{10}Be with an energy of 7 MeV. `Q.xls` gives the equilibrium charge state distribution for a carbon foil, but there should be not much difference to silicon nitride which is used in the present work. It suggests that 66% of the ions end up in charge state $^{10}Be^{3+}$. However it also says that higher charge states can be achieved with a gas stripper. This paradoxical result suggests that the input may be beyond the limits of the model and the result has to be taken with caution.

There are no experimental data for the stripping of beryllium at such high energies. Shima and Mikumo [1986] list data for ^{9}Be up to 4.1 MeV, which scales to 4.6 MeV for ^{10}Be.

Improved charge-state formulas have been proposed by Schiwietz and Grande [2001]. Figure 2.3 shows the mean-charge data from Shima and Mikumo [1986] where available, and the results of the model of [Schiwietz and Grande, 2001] up to 8 MeV for ^{9}Be. It is not clear which of the charge states is populated most at 7 MeV.

2.4 Simulations

In order to get a better image of the ion optical circumstances and possibilities, I decided to do computer simulations of various setups. The simulations allow a preview

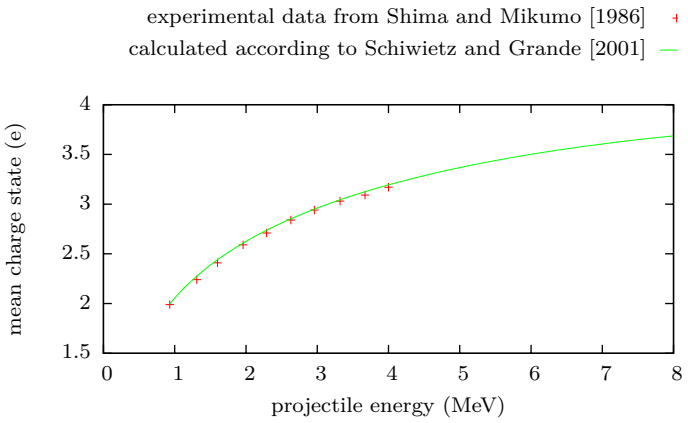

Figure 2.3: The mean charge of ^{9}Be after passing a carbon foil. The mean charge state is given in units of the elementary charge e.

of the expected suppression of boron and the transmission as well as the visualization of ion trajectories. This helps with the choice of a proper setup.

There is an ion optics simulation program called Prillion in use at VERA. It is written in Mathematica and based on a linearized matrix formalism [Banford, 1966].

There are some features that Prillion lacks:

- the output of a transmission
- the simulation of stopping and stripping in a foil

Instead of implementing the above features into Prillion, I have decided to write my own simulation code with a focus on my specific needs.

I wrote it in the C programming language, which gives flexibility and speed.

My program is in a large part based on matrix formalism, too, but it implements non-linear elements like apertures and stripping foils as well as the linear ion optic lenses and analyzing elements. For simplicity and flexibility, I did not implement the reading of a configuration file. This means that the setup is defined in the source code and the program has to be recompiled for each new simulation, but the compilation is very fast, because the program is small.

Without going too much into details of the implementation, I want to explain the simulation of stripping foils. I do a kind of Monte-Carlo simulation, but instead of doing a simulation of the scattering and degrading process on my own, I just reuse the output of TRIM [Ziegler and Biersack, 2003]. I use the output of ion energies and

scattering angles for the target foil of interest. I prepared TRIM simulation data for various $Si\,N_x$ foils with a large number of sample ions each.

The charge state of the ions behind the foil can be set to a fixed value and to the equilibrium charge state distribution optionally. For the comparison of the various setups, I use a fixed charge state to avoid confusion, as the charge state distribution is independent of the chosen setup. Efficiencies displayed in this section will have to be multiplied with the stripping yield, except for the setups using the Wien filter.

Apertures and slits stop the simulation of ions that cannot pass. The program outputs the ion paths and the transmission. The transmission is the ratio of ions that have passed the beamline over the total number of ions. To simulate the detector window, there are slits at the end of the simulated beamline. Ions passing these slits can be assumed to be counted in the detector.

For the calculation of the transmissions of each setup I simulate 10^4 ions of beryllium and boron each. The plots of ion trajectories that I will show on the following pages show only the trajectories of 100 ions of each species.

2.4.1 Definitions

For the following discussion of ion optics, I will denote the direction of the ion beam with the z-axis, the horizontal deviation of the ideal path is denoted with x and the vertical deviation with y. Note that when looking in beam direction, the x-axis is pointing rightwards and the y-axis is pointing upwards. Therefore the coordinates are left-handed.

The derivatives of x and y with respect to z are denoted by x' and y', respectively. Generally, the path of an ion can be described by a curve in a six dimensional phase space, where the six dimensions are the components of the three-dimensional vectors for the position and the momentum of the ion: x, y, z, p_x, p_y, and p_z. However, in ion optics it is convenient to use the quantities x, x', y, y', z, and p_z or Δp_z. These quantities can be derived from the phase space quantities in a well defined way.

$$x' \equiv \frac{\mathrm{d}x}{\mathrm{d}z} = \frac{\frac{\mathrm{d}x}{\mathrm{d}t}}{\frac{\mathrm{d}z}{\mathrm{d}t}} = \frac{m\frac{\mathrm{d}x}{\mathrm{d}t}}{m\frac{\mathrm{d}z}{\mathrm{d}t}} = \frac{p_x}{p_z}, \qquad y' \equiv \frac{\mathrm{d}y}{\mathrm{d}z} = \frac{\frac{\mathrm{d}y}{\mathrm{d}t}}{\frac{\mathrm{d}z}{\mathrm{d}t}} = \frac{m\frac{\mathrm{d}y}{\mathrm{d}t}}{m\frac{\mathrm{d}z}{\mathrm{d}t}} = \frac{p_y}{p_z} \tag{2.9}$$

In the following, the set of these convenient quantities will sometimes be referred to

as “phase space”. In general, Liouville’s theorem does not apply to this “phase space”.

2.4.2 Initial beam properties

The simulations start with an ion beam as it can be expected at the position of the `L4-1` slits of VERA, which is 40 cm before the insertable Si-detector (cf. figure 2.6 on page 26). We assumed the beam width to be approximately ±2 mm and the divergence to be approximately ±2 mrad. I use a pseudo-random number generator to simulate the initial beam. The starting points of the ions are distributed uniformly inside a four dimensional phase-space hyper-ellipsoid. Figure 2.4 shows projections of the simulated phase space.

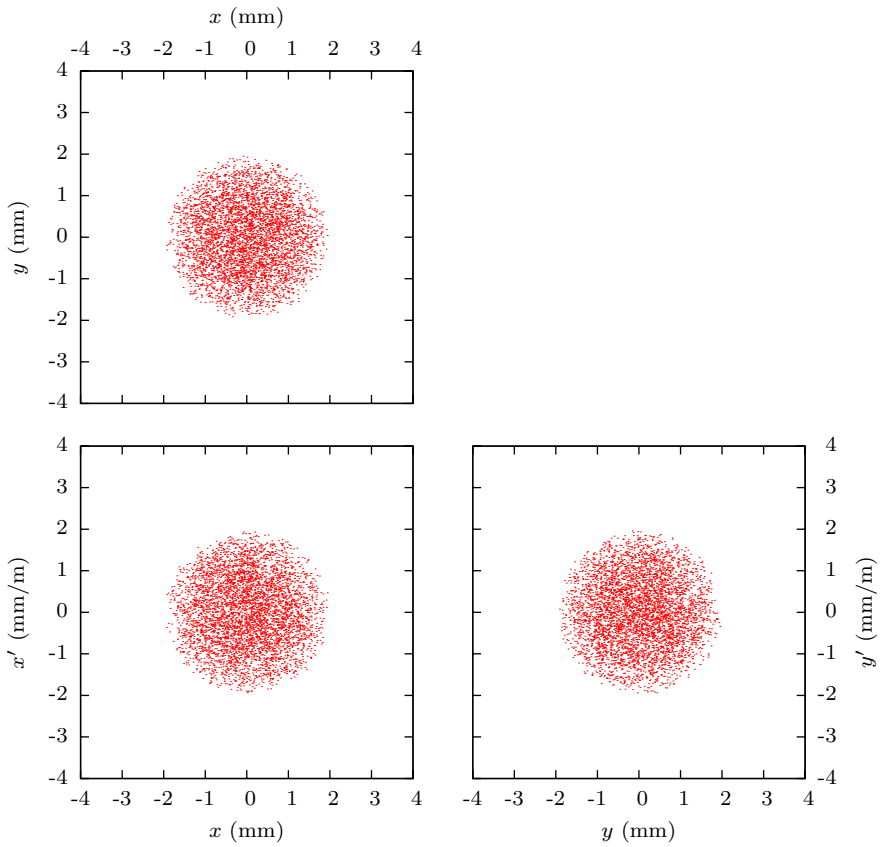

Figure 2.4: Phase-space diagrams of the simulated beam at the position of `Slt L4-1`. The dots represent the phase-space positions of 5000 simulated ions. The diagrams show three projections of the phase-space slice at the initial position.

The initial beam is monoenergetic in the simulation, because the energy distribution of the incident beam is narrow compared to the energy distribution of the degraded beam behind the foil.

2.4.3 Setups involving the Wien filter

VERA has a Wien filter which is scarcely used for the lower mass isotopes since a high energy ESA has been added to the beamline. A Wien filter allows the passage of all charge states of the selected velocity, therefore I considered it interesting enough to incorporate it into simulations.

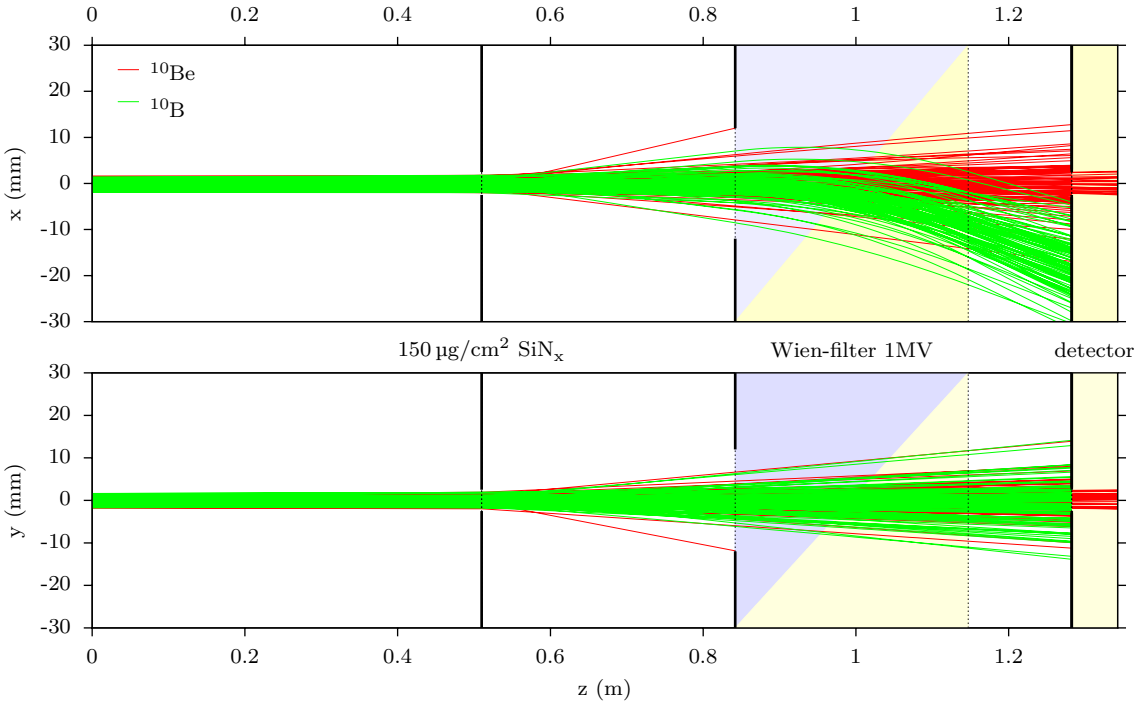

Figure 2.5: A setup using an extremely strong Wien filter. While the geometry of the Wien-filter is the geometry of the Wien-filter present at VERA, the electric field in this simulation is 63 MV/m. The transmission is 27% for beryllium and 2‰ for boron.

The Wien filter is a velocity filter. It consists of an electric field perpendicular to a magnetic field. With appropriately chosen field strengths the Coulomb force of the electric field cancels out the Lorentz force of the magnetic field on the ion for a

desired velocity. This effect is independent of the ion's charge, because both forces are linear in charge.

The force on an ion of the mass m and the charge q is

$$m\ddot{x} = q\,(\mathcal{E} - vB) \tag{2.10}$$

if we assume the electric field $\mathcal{E}$ is in the direction of the x-axis and magnetic field B in the direction of the y-axis. The path therefore satisfies the differential equation

$$\begin{aligned} x'' &= \frac{\ddot{x}}{v^2} = \frac{q}{mv^2}\,(\mathcal{E} - vB) && (2.11)\\ &= \frac{q}{mv^2}\,(\mathcal{E} - (v_0 + \Delta v)B) \\ &= \frac{q\Delta v}{mv^2}B && (2.12) \end{aligned}$$

where $v_0 = \frac{\mathcal{E}}{B}$ and $\Delta v = v - v_0$. Thus ions passing through a Wien filter at the velocity v_0 ($\Delta v = 0$) behave the same way as in free drift. This is independent of the charge. The separation on the other hand depends on the charge. Neutral particles cannot be separated by a Wien filter.

Using the Wien filter for the separation of ^{10}B and ^{10}Be after the stripping foil sounds interesting for the feature of the Wien filter that it could let pass all charge states of ^{10}Be after post-stripping.

Figure 2.5 shows the simulation of a simple setup with the Wien filter. The simulation may look promising, the short length of the beam line minimizes the loss due to angular straggling. The transmission is 27% for beryllium and 2‰ for boron. However, this setup would require an electric field of 62 MV/m and a magnetic field of 5 T. This is far beyond the limits of the Wien filter.

Separation with the Wien filter requires a longer beam line. Therefore we need focusing elements. The focusing however depends on the charge of the ions. Figure 2.6 shows a setup that uses a magnetic quadrupole doublet for the focusing. The transmission is 27% for beryllium and 3% for boron.

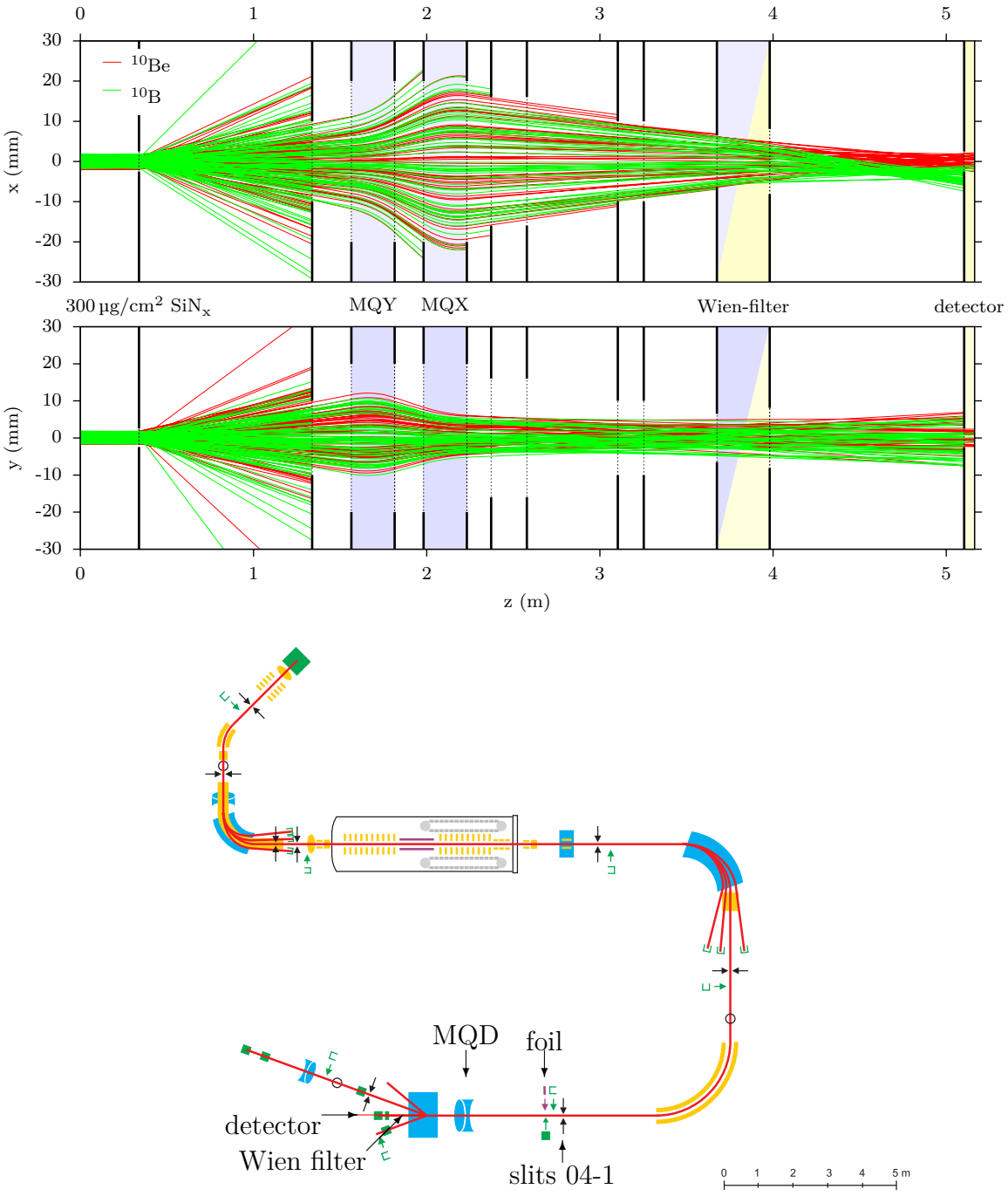

Figure 2.6: A setup using a realistic Wien filter and the magnetic quadrupole doublet. The quadrupole doublet is in the position that we have it now and the Wien-filter would be placed at the 0 °-port of the switching magnet. In the simulation the transmission is 27% for beryllium and 3% for boron.

2.4.4 Setups using the ESA 04

The force acting on an ion in an electrostatic field is $q\vec{\mathcal{E}}$. The electrostatic analyzer consists of two concentric spherical electrodes. The ideal path of the ions is a circular arc. The spherical shape of the electrodes makes the ESA double focusing, i.e. focusing in horizontal and vertical direction. The equation of the centripetal force $\frac{mv^2}{r}$ and the electrostatic force gives

$$\begin{aligned} q\mathcal{E} &= \frac{mv^2}{r} \\ rq\mathcal{E} &= 2\frac{mv^2}{2} \\ r\mathcal{E} &= \frac{2E}{q}, \qquad \text{where } E = \frac{mv^2}{2} \end{aligned} \tag{2.13}$$

The high energy electrostatic analyzer (ESA) has the highest energy separation available at VERA. It has a radius of 2 m. In order to achieve a spatial separation of 5 mm at an image distance of 2.4 m, the $\frac{\Delta E}{E}$ has to be 1.1‰ only. Generally, high energy separation has a downside: if the separation is in the range of the energy straggling of the beam, the detector will only see a portion of the beam. Thus, energy separation above the separation needed to suppress the ^{10}B background should be avoided.

If the ESA is to be used as an analyzer after the post-stripping, then the foil should be very thin in order to minimize energy straggling. Figure 2.7 shows a simulation of a setup with a 30 µg/cm^2 SiN_x foil. The transmission is 46% for beryllium and no boron is transmitted in the simulation.

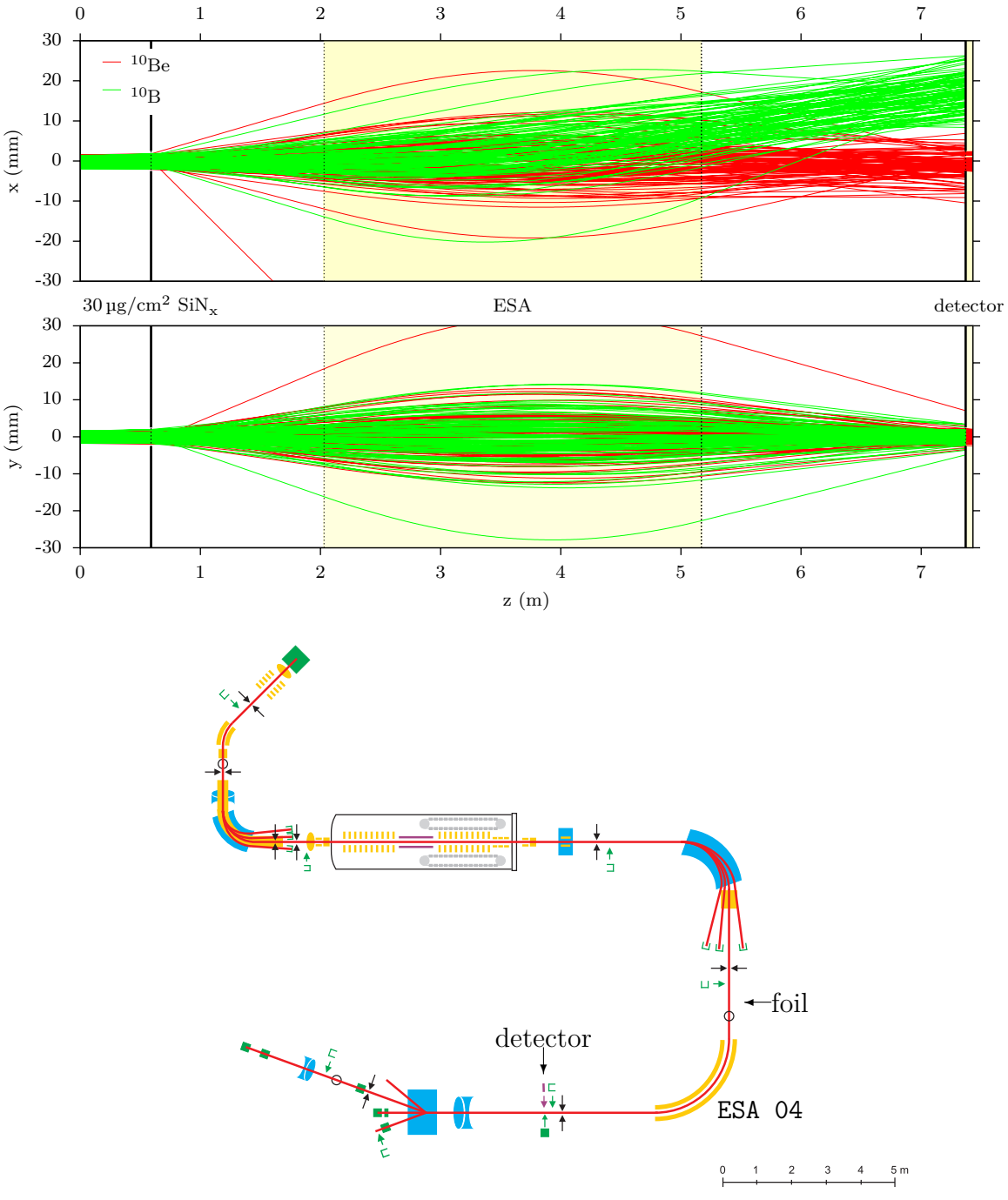

Figure 2.7: A setup using the ESA. The transmission is 46% for beryllium and no boron is transmitted in the simulation.

2.4.5 Setups using the switching magnet

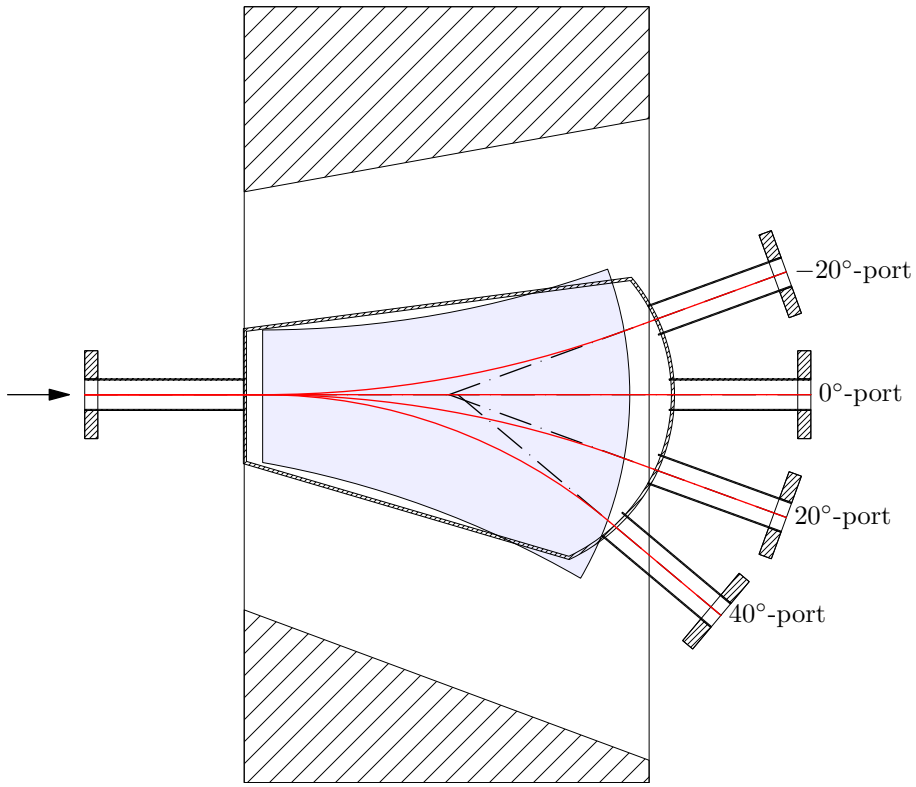

Figure 2.8: This is a sketch of the switching magnet `BM 04-1`. The magnetic field is shown in light blue. In principle it has the shape of a half disk: the edge of the field is perpendicular to the beam direction at the entrance. The shim angle at the exit is half the angle of the port. The red lines show the ideal beam paths for the four exit ports.

The switching magnet (figure 2.8) has a medium energy resolution, which is about 1-2%.[3] There is a magnetic quadrupole doublet just before the switching magnet, which gives flexibility in the choice of the detector position (see figure 2.10).

As the switching magnet is the analyzing element that we have used in the experiments, I will briefly explain the ion optics of a switching magnet. Figure 2.9 shows a schema of a switching magnet. The magnetic field is perpendicular to the drawing plane and homogeneously extends over a half disk of radius R. The beam enters the switching magnet perpendicular to the edge of the field, thus with zero shim angle.

[3] In order to achieve a spatial separation of 5 mm at an image distance of 1 m, the $\frac{\Delta E}{E}$ has to be 1% when bending 40° and 2% when bending 20°.

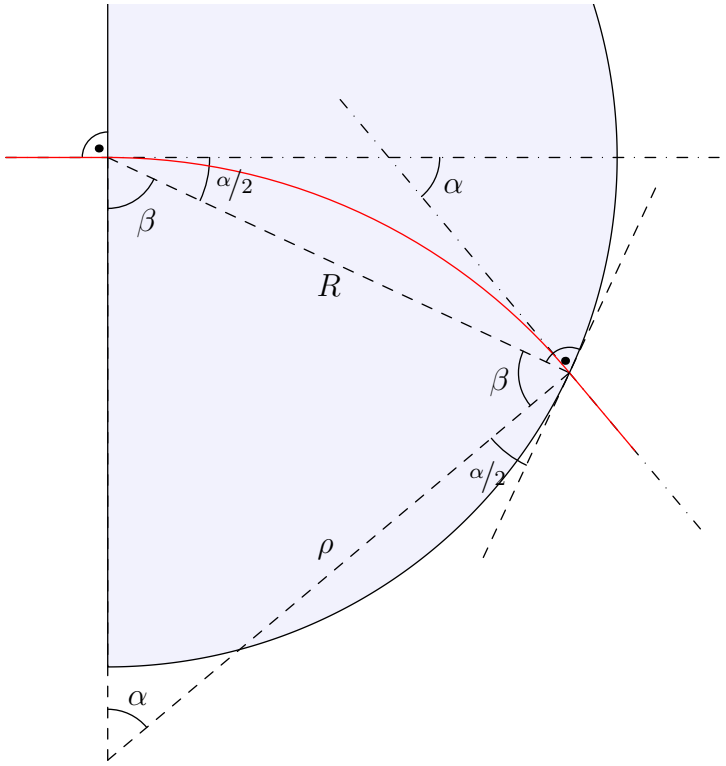

Figure 2.9: A schematic drawing of the switching magnet geometry. The magnetic field has the shape of a half disc with the radius $R = 0.48\,\mathrm{m}$. If α is the desired deflection angle, the exit port has to be located at an angle of $\alpha/2$ off the straight line. Because the magnetic field is homogeneous, the beam path is an circular arc. The shim angle at the exit of the magnetic field is $-\alpha/2$.

The beam path in the region of the magnetic field is a circular arc with the radius ρ. The radius is related to the magnetic field and the magnetic rigidity of the beam by equation (2.14). The relation between the bending radius ρ and the deflection angle α is given by equation (2.15).

$$B\rho = \sqrt{\frac{2ME}{Q^2}} \tag{2.14}$$

$$\frac{\rho}{\cos \alpha/2} = \frac{R}{\sin \alpha} \tag{2.15}$$

($M \ldots$ ion mass, $E \ldots$ ion kinetic energy, $Q \ldots$ ion charge)

The entrance point, exit point, and the center of the arc span an isosceles triangle. The angle β in figure 2.9 can therefore be derived from the sum of angles $\pi = \alpha + 2\beta$

as $\beta = \pi/2 - \alpha/2$. Finally, the exit shim angle is $\beta - \pi = -\alpha/2$. Because the shim angle is negative, the edge will act defocusing on the horizontal motion and focusing on the vertical motion. For small angles α this effect is half of the focusing effect of the bending field. Thus, in total the switching magnet is double focusing in x and y; it is even stigmatic for small angles.

I have simulated various setups with the switching magnet at $-20°$ and $40°$ with various foils and various positions for the foils and the detector. Figures 2.10 and 2.11 show optimized setups for the two switcher ports.

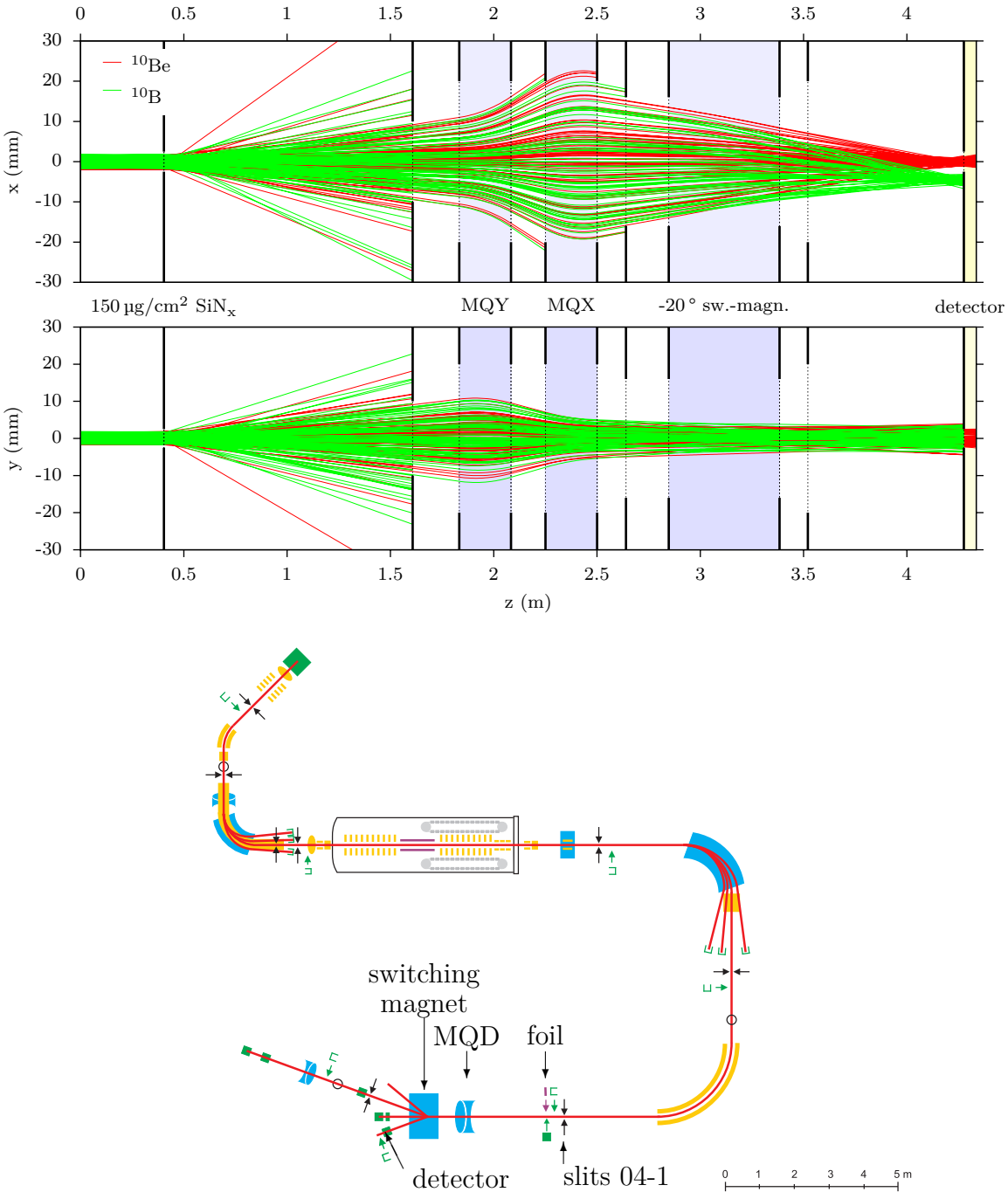

Figure 2.10: A setup using the $-20°$ beam line. The transmission is 51% for beryllium and $5 \cdot 10^{-4}$ for boron. MQX and MQY denote the magnetic quadrupoles which together form the magnetic quadrupole doublet (MQD). The MQY is focusing in the y-direction and defocusing in the x-direction. For MQX it is just the opposite.

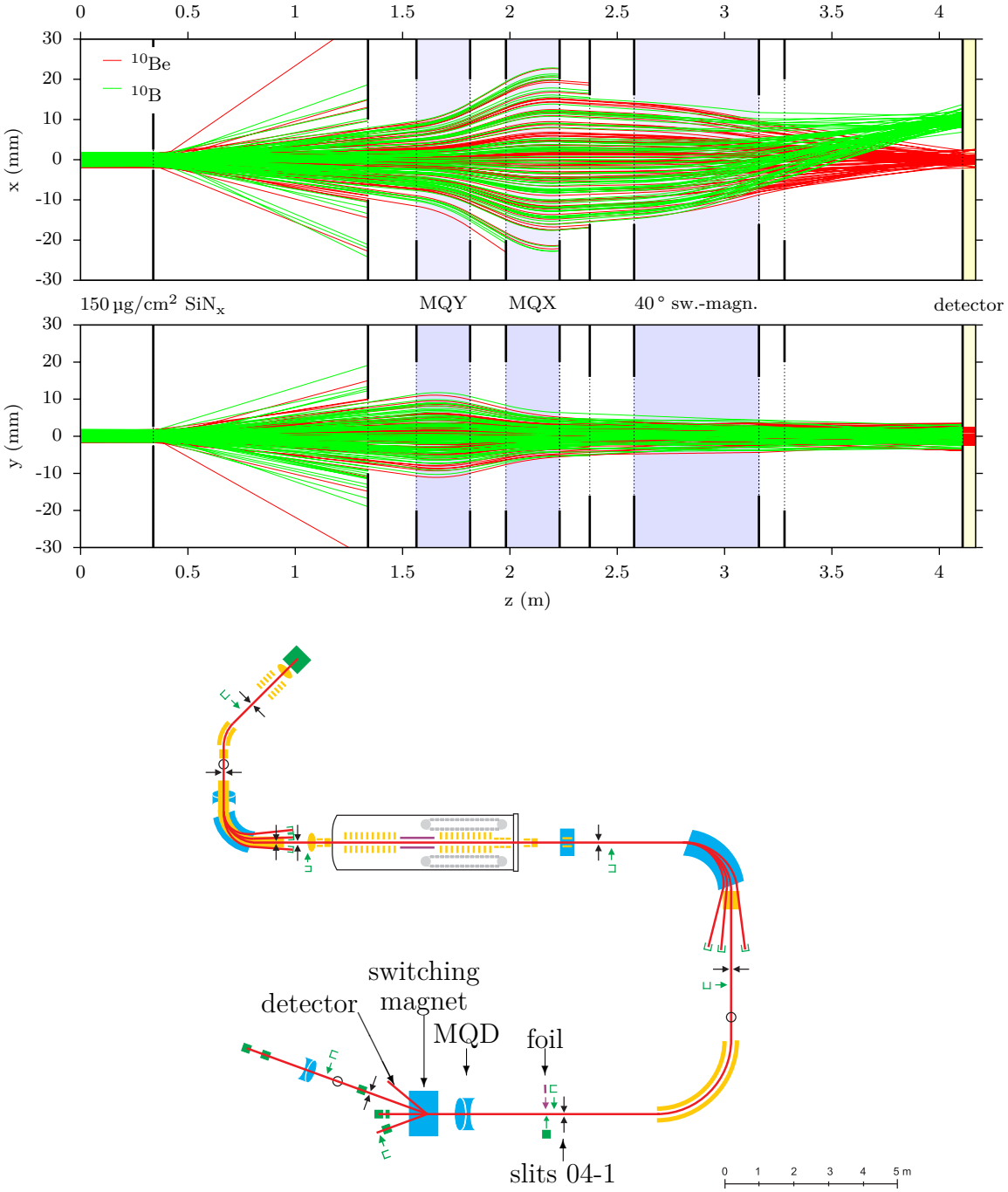

Figure 2.11: A setup using the 40° beam line. The transmission is 59% for beryllium and no boron is transmitted in the simulation.

2.5 Summary

Table 2.2 summarizes the results of the simulations. There are some uncertain parameters in the simulation, the most important being the emittance and the phase-space distribution of the beam delivered by the accelerator.

setup	SiN_x foil	background	transmission
Wien filter (figure 2.6)	$300\,\mu g/cm^2$	3%	21%
ESA (figure 2.7)	$30\,\mu g/cm^2$	0	46%
20° switcher (figure 2.10)	$150\,\mu g/cm^2$	0.5‰	51%
40° switcher (figure 2.11)	$150\,\mu g/cm^2$	0	59%

Table 2.2: Summary of the simulation results. These are the results of the simulations presented above. More simulations have been carried out. This list just gives the results of good setups for each of the four possible analyzing components. The last column shows the ion optical transmission of the simulation, but it does not include the transmission in the accelerator and the stripping yield for the selected charge state after post-stripping.

The simulations suggest that using the 40° port of the switching magnet, gives the best efficiency. However, at the time of my first experiments, the 40° port was occupied by a PIXE setup. Finally we decided to use the second best simulated setup and use the −20° port of the switching magnet. For the first experiments I prepared two silicon nitride foils with a thickness of 500 nm and 1000 nm. Assuming a density of $3\,g/cm^3$ for silicon nitride, this corresponds to area densities of $150\,\mu g/cm^2$ and $300\,\mu g/cm^2$ respectively.

3 Experimental setup

3.1 Beam line setup

We have done measurements with two different setups. Basically there is not much difference between the two setups. For the first measurement we had the chance to use the position of the first ΔTOF start detector while the ΔTOF detector was under maintenance. The detector position is in the `L5` beam line behind the 20°-port of the switching magnet. Later we had to build our own beam line—beamline section `L8`—at the −20°-port of the switching magnet. The 20°-port and the −20°-port have equivalent resolution.

Yet, we have not tried experimentally setups using the ESA 04, the 40°-port of the switching magnet, or the Wien filter.

3.1.1 Foils used for post-stripping

I inserted a feed-through with a fastener for the post-stripping foils into the six-way cross in beamline-section `L4`, which also contains the surface barrier detector for ^{14}C measurements. (See figure 3.2.) A linear motion feed-through allows us to retract the foils and choose one of three positions of foils or foil stacks. Therefore it is possible to try several foil thicknesses without venting the beam line.

3.1.2 The beamline section `L8`

Before, the `L8` beam line had been used in cooperation with the Stefan Meyer Institute (SMI) for PIXE measurements for the quality control of particle detectors.

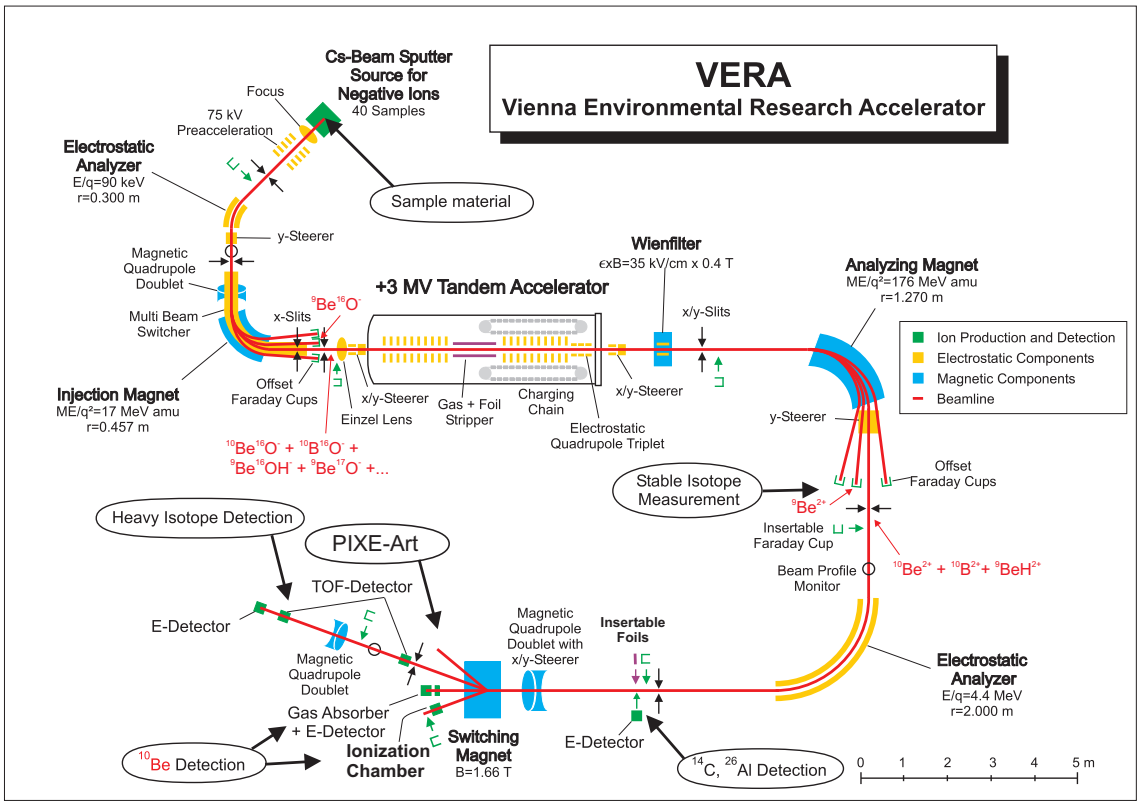

Figure 3.1: VERA in February 2006. This figure is based on a figure by Vockenhuber [2004].

		rel. pos. (cm)	pos. (m)
Switching magnet	drift length	20.7	32.094
	arc length	53.6	32.630
	drift length	13.7	32.767
	total length	88	32.767
Gate valve L8	center	3.5	32.802
	total length	7.0	32.837
Bellows	total length	27	33.107
Drift tube	total length	36.8	33.475
Cross (6 way)	aperture	8.6	33.561
+ detector	center	13.5	33.610
	total length	27	33.745
Faraday-cup	total length	31.7	34.062

Table 3.1: The dimensions of the L8 beam line in February 2006: The third column shows the position relative to the beginning of the part, the rightmost column shows the position of the end of the component relative to the ion source.

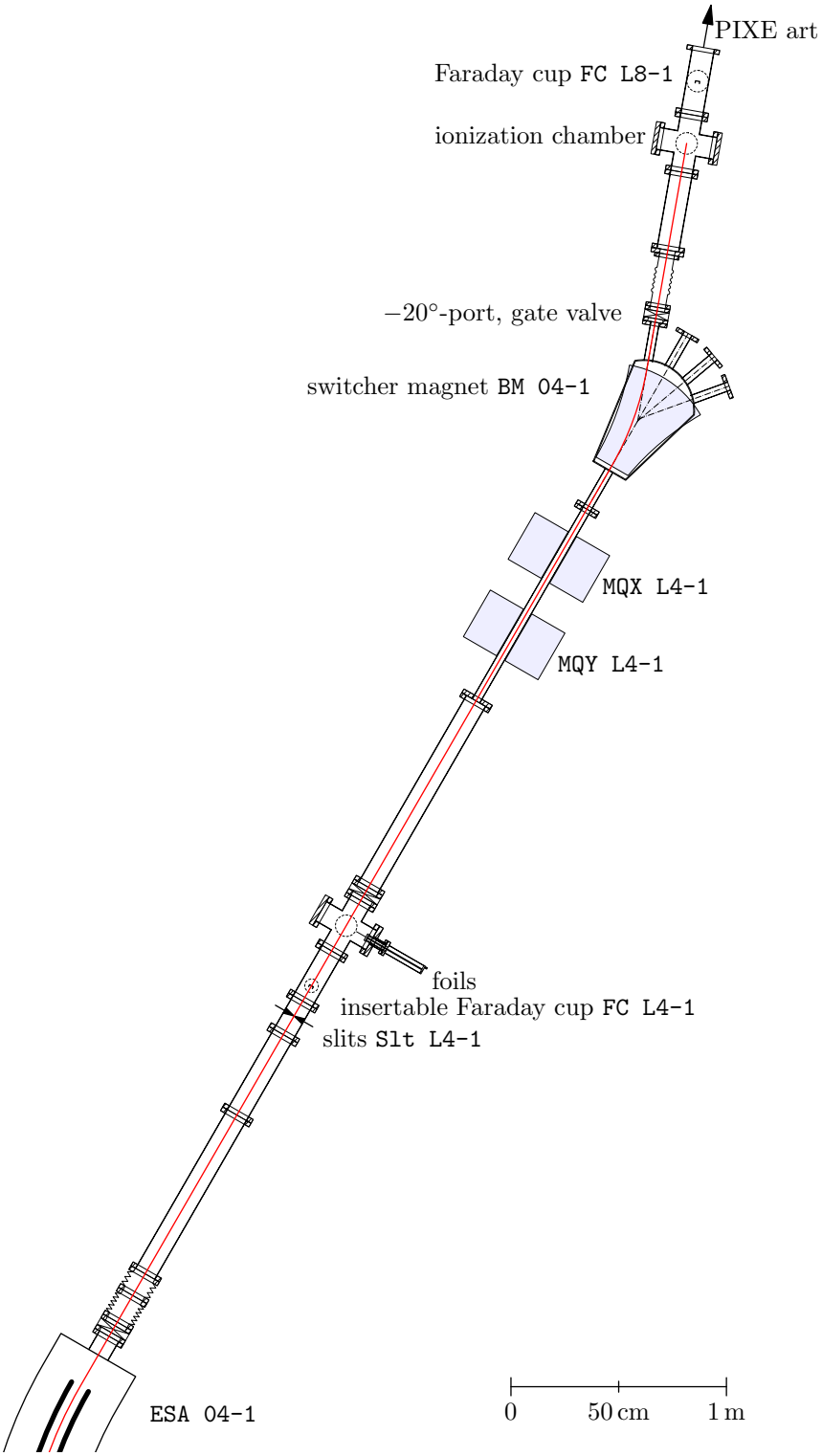

Figure 3.2: This figure shows the VERA beamline sections L4 and L8. The red line shows the ideal path of the ion beam.

We replaced the SMI beamline with our new beam line for ^{10}Be and "PIXE art".[1] The beamline was aligned with a plummet above the switching magnet and the bottleneck of the switching magnet port using a theodolite.

Figure 3.1 shows the VERA setup with our new `L8` beam line, table 3.1 gives the geometry of the `L8` beam line, and figure 3.2 shows the section from the ESA to the `L8` beamline in more detail. Later the "PIXE art" equipment was removed from the 40°-port and appended to the `L8` beam line.

3.2 The ionization chamber detector

We used a new ionization chamber built in our laboratory by Oliver Forstner. Our ^{10}Be measurements were the first measurements that used the new ionization chamber in an AMS measurement at VERA [Forstner et al., 2007]. The ionization chamber is based on a design that was developed at the ETH Zurich [Döbeli et al., 2004; Grajcar, 2005].

The detector fits into a DN 100 cross pipe and is mounted on a linear motion feed-through, so it can be retracted to allow the beam to pass. A plate with two apertures—3 mm and 6 mm in diameter—is attached to a second feed-through. The apertures can therefore be inserted even if the detector itself is retracted. The entrance window of the detector is a 5 mm × 5 mm × 100 nm silicon nitride foil from Silson.[2]

The ionization chamber is filled with isobutane gas. The gas is led into the ionization chamber via a needle valve that is set manually. It is pumped out constantly via another needle valve which is controlled by a PID-controller to keep a constant pressure.

The detector has two anodes and two pre-amplifiers. Anode 1 is located above the front section of the detector and anode 2 above the back section. Therefore, the signal at anode 1 corresponds to the energy deposited in the front section and the signal at anode 2 corresponds to the energy deposited in the back section of the ionization chamber. If the ion is stopped in the active region of the ionization chamber, the sum

[1] The "PIXE art" team wanted to use the −20°-beamline as there is more free space around and it is near to a door, which is useful for their handling of precious works of art.

[2] Silson Ltd, JBJ Business Park, Northampton Road, Blisworth, Northampton, NN7 3DW, England, `http://www.silson.com/`

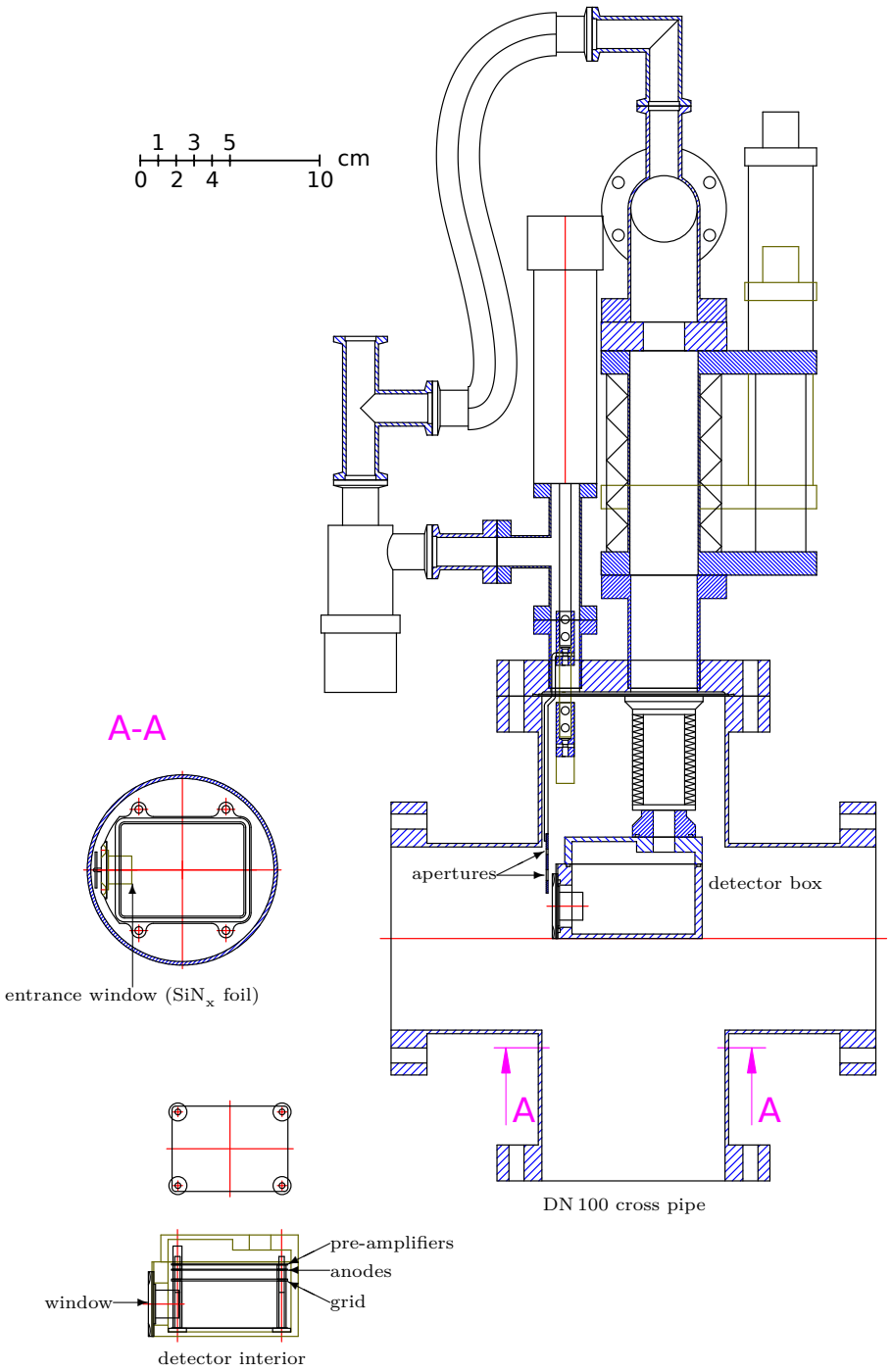

Figure 3.3: A true-to-scale drawing of the new ionization chamber. The ionization chamber as well as the drawing is a work of Oliver Forstner. [Forstner et al., 2007]

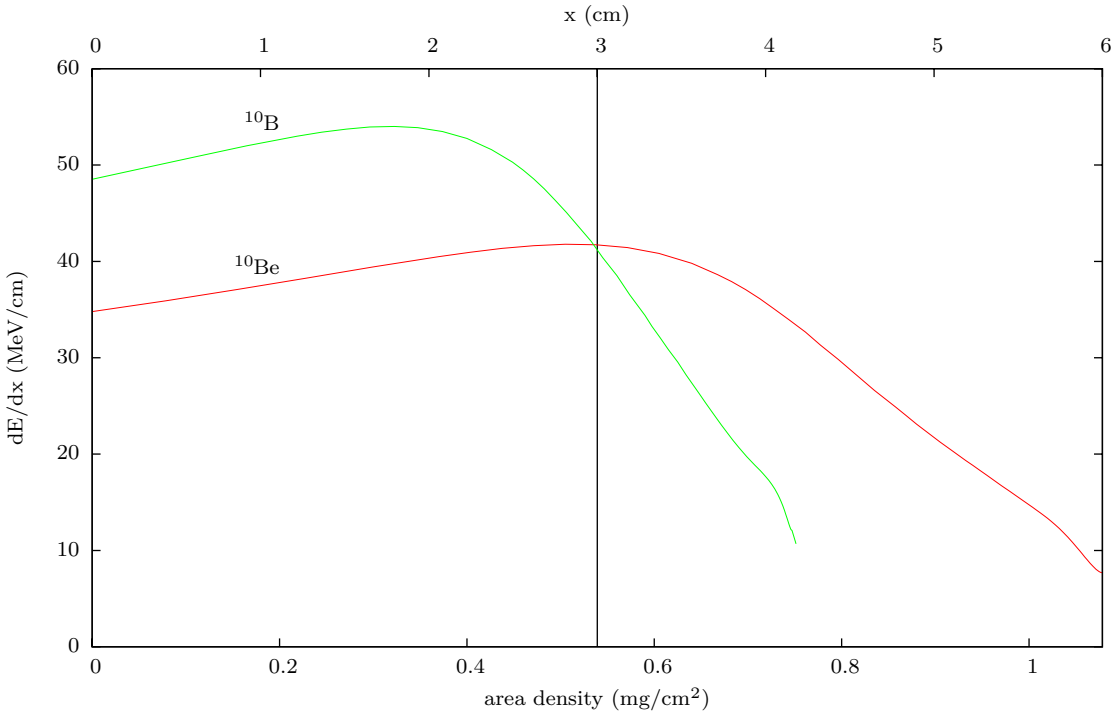

Figure 3.4: The energy-loss curves for ^{10}Be and ^{10}B in the ionization chamber filled with isobutane gas at a pressure of 73 hPa and a temperature of 20°C. Data from SRIM [Ziegler and Biersack, 2003].

of the energies deposited in both sections of the chamber is the total energy of the ion minus the energy loss in the entrance window.

The stopping power of isobutane for ^{10}B is higher than for ^{10}Be, therefore the ^{10}B ions lose a bigger fraction of their energy in the front section of the ionization chamber than the ^{10}Be ions. The ^{10}Be ions appear to the upper left side of the ^{10}B peak in the ΔE_1–ΔE_2 spectrum.

Figure 3.4 shows the energy-loss curves for beryllium and boron in the ionization chamber. With a good choice of the gas pressure, the energy-loss peak for boron lies in the sensitive volume of the first anode, while beryllium extends farther into the sensitive volume of the second anode.

Figure 3.5 shows a two-dimensional spectrum of a ^{10}Be measurement run with a gas pressure of 95 hPa. It was measured for 82.4 s, 353834 events were counted, and 3017 of them were identified as ^{10}Be.

The different stopping power allows a clear discrimination of ^{10}Be and ^{10}B. The

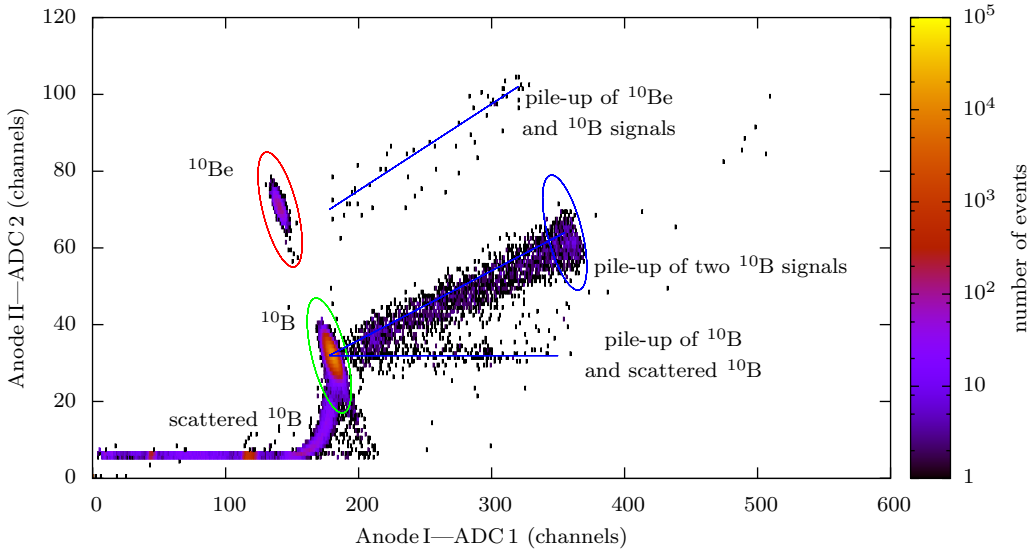

Figure 3.5: The spectrum of a single run on a S555 standard cathode (run 484 in measurement Be_ng1_poststrip). The ^{10}Be peak is well isolated from the background. Most of the background is ^{10}B, as expected. The other background is mostly because of pile-up signals. Some boron is scattered by the residual gas in the beamline and produces low energy tails.

signal at anode 2 (in ADC 2) alone would allow a discrimination of the main peaks of ^{10}Be and ^{10}B, but the pile-up of two ^{10}B signals gives signals in ADC 2 that would be counted as ^{10}Be. A two-dimensional bin around the ^{10}Be peak avoids this background.

3.2.1 Signal processing

The processing of the signals involves two processing lines, one for each detector anode. A signal processing line consists of a pre-amplifier, a main amplifier and an analog-to-digital converter. Further there is a gate generator which is triggered by the signal of the main amplifier for anode I (see figure 3.6). The two pre-amplifiers for the detector are inside the detector box just above the detector anodes. The signal path of the high impedance detector signal to the pre-amplifier is very short, therefore. The signals of the pre-amplifiers are transferred over a 50 Ω line to the main amplifiers.

The signal from the main amplifiers is led to the multi-channel ADC. The gate signal is a rectangular signal with a duration of $\tau_g = 2\,\mu s$. The gate signal activates

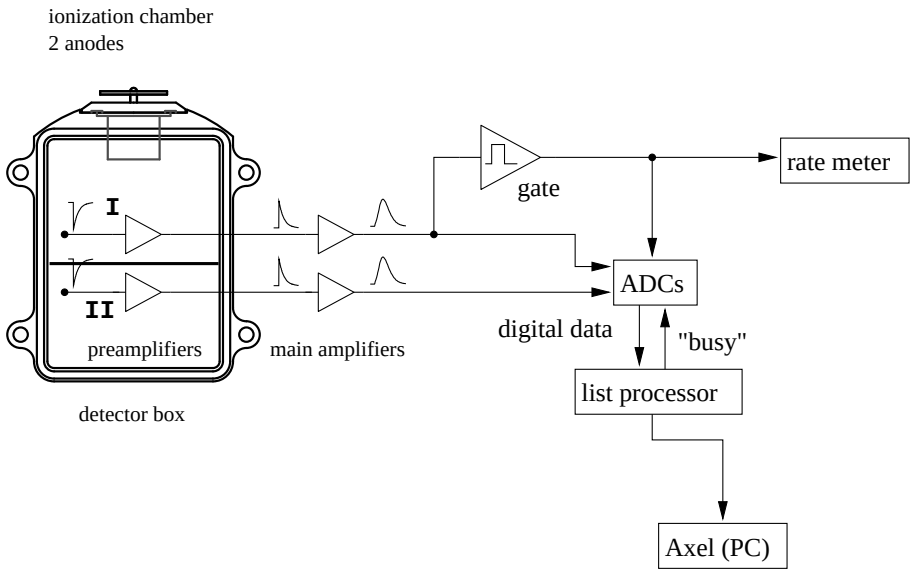

Figure 3.6: This is a simplified schematic drawing of the detector signal processing. "Axel" is a personal computer that controls the accelerator and collects data during the measurement.

the ADC. At the end of the gate signal, the ADC reports the maximum voltage of the input signal to the list processor. We have chosen this short gate time so that only one signal fits into the gate time. Otherwise, if the gate time is longer than the signal width, two signals arriving while the gate is active will be separated. The ADC will select the higher signal, regardless of the order of the two signals. For example ADC 1 will report the voltage of a ^{10}B signal while at the same time ADC 2 will report the voltage of a ^{10}Be signal. Also the suppression of signal pile-up depends on the gate time. See section 3.2.3.

3.2.2 Dead time

After the end of the gate signal following each detector event the list processor is busy for $\tau_b = 16\,\mu s$. (This time depends on the program that the list processor is loaded with.) During this time, the ADC is put on hold. A detector event that happens while the ADC is put on hold may trigger a new gate signal, but it will be not be tracked by the ADC. The ADC will track events only if the gate signal starts after

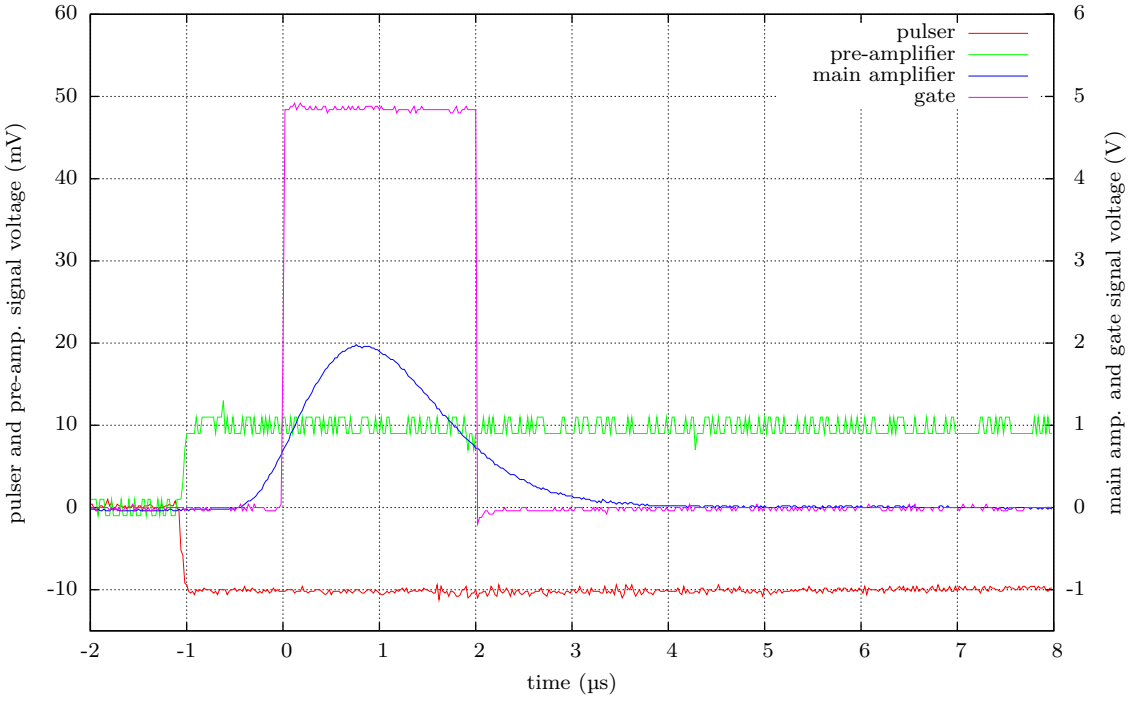

Figure 3.7: Detector and amplifier signals in response to a test signal from a pulse generator. The signals were acquired with an oscilloscope. Pulser and pre-amplifier signals are drawn with respect to the left scale, main amplifier and gate signals with respect to the right scale. The signals have been synchronized with the gate signal.

the ADC has been cleared. Therefore the total dead time is

$$\tau = \tau_\mathrm{g} + \tau_\mathrm{b} = 18\,\mu\mathrm{s} \tag{3.1}$$

because two consecutive signals with an interval of 18 µs or longer will be detected both. I have confirmed this behavior of the data acquision electronics using a double pulse generator.

In the data evaluation the dead time is corrected by subtracting the sum of the dead times $N\tau$ for N events from the measurement time T. Hence the real rate of events is estimated as $\frac{N}{T-N\tau}$. I assume a non-paralyzable behavior of the detector, i.e. detector events during dead time will not restart the dead time. The electronics has a paralyzable behavior, if the interval of successive events is shorter than the gate time, because the gate signal—which is generated by an Ortec CO4020 Quad 4-input

logic—can be extended. I disregard this behavior in the dead-time correction, the error is in the order of $\tau_g \cdot \frac{N}{T}$.

3.2.3 Signal pile-up

Since the amplifier output signal has non-zero duration, the two signals of events with a short time offset Δt may give a sum signal which cannot be resolved to two signals by the data acquisition equipment and impedes counting of either of the two signals. This effect is called pile-up. Generally there are two kinds of pile-up: tail pile-up and peak pile-up [Knoll, 1979].

In the case of tail pile-up, the first signal is acquired without any modification, but the tail of the first signal adds to the second signal. As long as we don't consider situations involving more than two detector events, tail pile-up does not have an influence on our measurements, because the dead time of 18 µs is long enough for the signal to return to the baseline. A signal influenced by tail pile-up will not be counted (cf. figure 3.8).

When the time between the two events is short enough for the second signal to interfere with the acquisition of the first signal, we speak of peak pile-up. The consequence of peak pile-up can be that neither of the two events can be identified and counted. Both are removed from the respective peak in the spectrum. As demonstrated in figure 3.8, the maximum time offset Δt for which no peak pile-up occurs, depends not only on the shape of the amplifier signal, but also on the relative height and the order of the two interfering signals. An analysis or correction of the peak pile-up is rather complicated. However, it is easy to estimate an upper bound for the number of signals that can be lost on account of peak pile-up: peak pile-up does not occur, if the time interval between two consecutive signals is larger than the gate time $\tau_g = 2\,\mu s$. From the Poisson distribution we get the probability that no event occurs within τ_g.

$$P_{r\tau_g}(0) = e^{-r\tau_g} \tag{3.2}$$

where r is the real rate of detector events. The fraction of events lost is therefore less than or equal to $1 - P_{r\tau_g}(0)$ (cf. Knoll [1979]). With the typical upper limit of $r = 1000\,s^{-1}$ this is about 2‰.

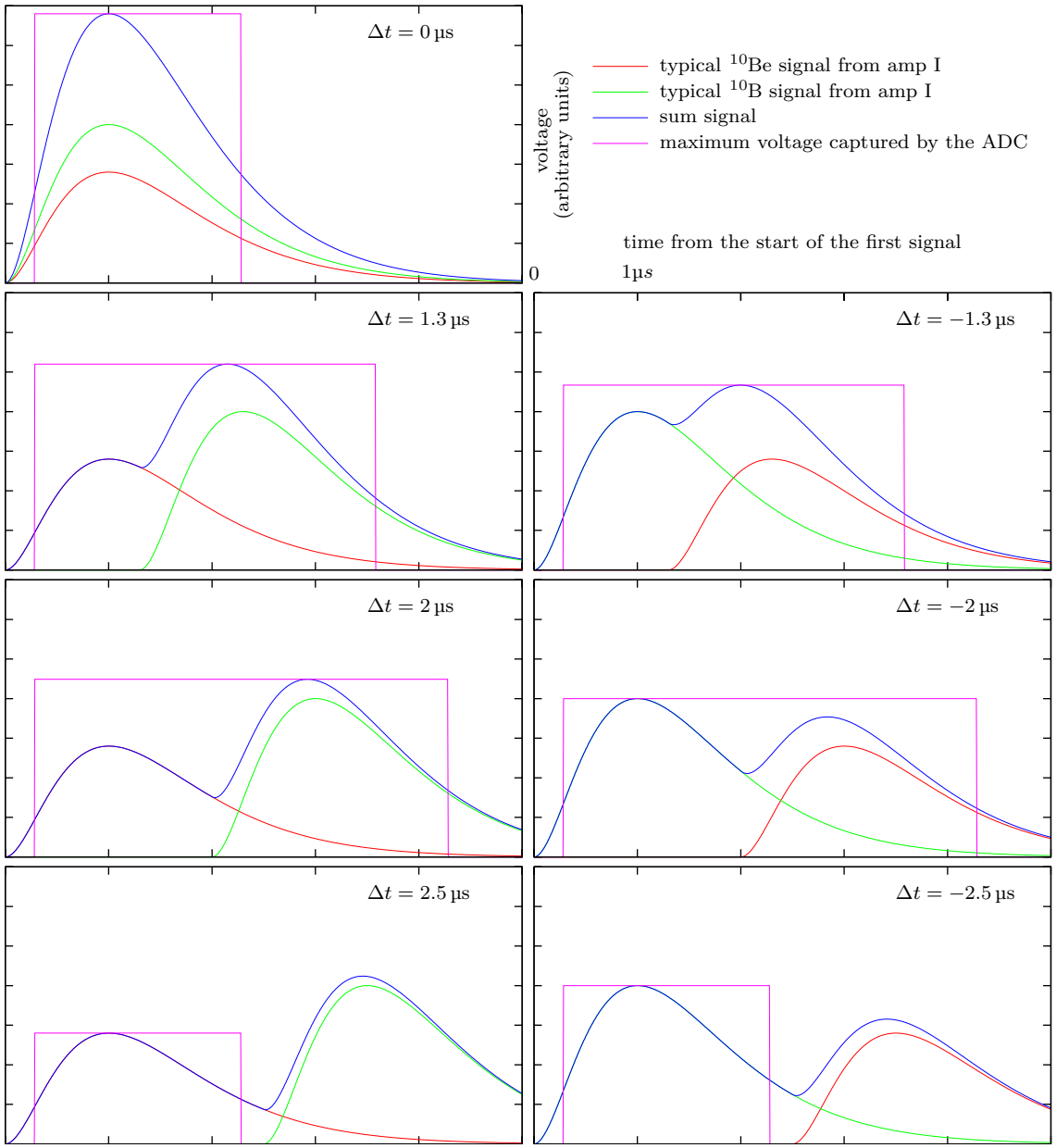

Figure 3.8: Five examples of peak pile-up and two examples of tail pile-up. The signals are typical input signals for ADC 1, ^{10}Be gives a smaller signal than ^{10}B. The examples show the signals resulting from one ^{10}Be and one ^{10}B ion arriving at the detector within the time interval $|\Delta t|$. The graph on top shows the situation without a time offset. Below, the three graphs on the left show the resulting signal of a ^{10}Be ion followed by a ^{10}B ion while the three graphs to the right show the analog situation with reversed order. A fourth line in the graphs symbolizes the active gate while the ADC tracks the signal, the height of the line is the voltage that the ADC finally reads. This figure illustrates that the value of the resulting digital signal not only depends on the absolute time offset, but also on the time order of the two events.

Pile-up involving more than two events is even more rare. The fraction of signals which will be followed by two other signals within the dead time τ is

$$1 - P_{r\tau}(0) - P_{r\tau}(1) = 1 - \mathrm{e}^{-r\tau} - r\tau\mathrm{e}^{-r\tau} \approx (r\tau)^2 = 4 \cdot 10^{-4}. \tag{3.3}$$

Even though the number of events lost on account of pile-up is low, pile-up events could add to counting background, if other events than the incident of a ^{10}Be ion appear in the spectrum at the place of the ^{10}Be-peak. Therefore—in context of a general effort to understand all the phenomena of the measured spectra—it is sensible to analyze the positions where pile-up events show up in the spectra.

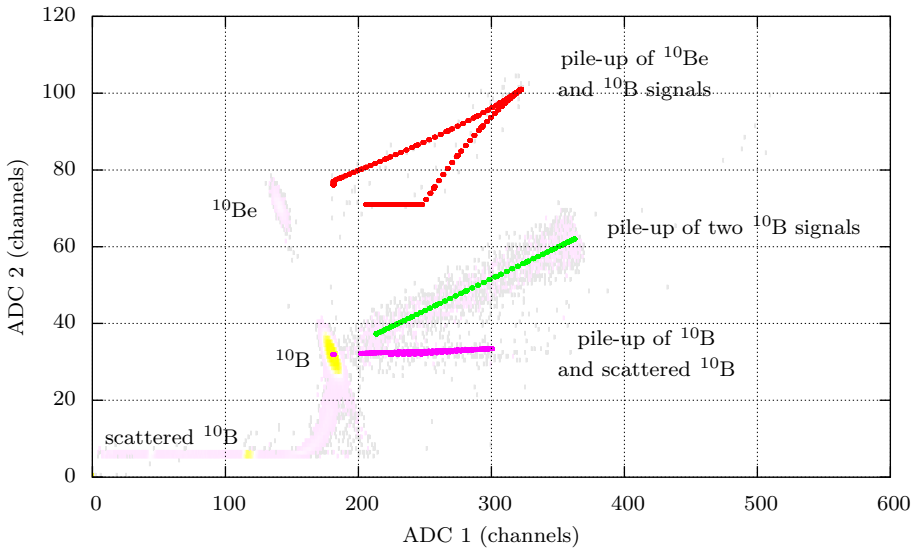

Figure 3.9: This figure shows the expected (simulated) positions of peak pile-up signals in the same spectrum as in figure 3.5. The effect of pile-up depends on the order of events, therefore there are two lines of B–Be pile-up. Five of the possible combinations of events are shown for a distribution of time interval Δt between the events.

Generally, in measurements with a single detector channel, pile-up can only be recognized by additional information on the signal, for example the pulse width. In the one-dimensional energy spectrum the pile-up counts can be anywhere in the range from the peak with the smallest energy to the peak of the sum of the energies of the contributing events. If the ion of interest has higher energy than the background ion, some signals of two background ions will be counted as a foreground ion if no pile-up suppression methods are applied.

In the case of the two dimensional spectrum of our ^{10}Be, the information of the two input channels suffices to suppress pile-up background. Figure 3.9 shows where the pile-up signals appear in the spectrum. The calculations are based on a simplified model for the shape of the amplifier signal:

$$f(t) = \frac{e^2}{4}\left(\frac{2t}{\tau_a}\right)^2 \exp\left(-\frac{2t}{\tau_a}\right), \tag{3.4}$$

where τ_a is the time for the signal to reach its maximum.

Another simplification is that the gate signal is triggered a fixed time offset before the signal peak. In reality, the time offset may depend on the signal amplitude. Further, with the Quad 4-input logic that generates the gate signal, the timing of the signal will not be completely reset by a second signal, e.g. the total duration of the gate signal triggered by two events with an interval of $\Delta t = \tau_g$ is shorter than $2\tau_g$.

The count rate of pile-up is proportional to the product of the count rates of the individual events. Most of the events in the detector root in ^{10}B ions, therefore most of the pile-up is double ^{10}B pile-up. Double ^{10}Be pile-up has not been observed, as it is rather rare.

3.2.4 ^{9}Be background

As explained in section 2.1.3 some ^{9}Be can reach the detector. It has $\frac{9}{10}$ of the energy of ^{10}Be. It can reach the detector only via scattering at the residual gas. (For example via charge change inside the switching magnet.)

Figures 3.10 and 3.11 show spectra where a number of ^{9}Be ions have been detected. The tail of ^{9}Be clearly shows a lower stopping power than ^{10}B, but it does not reach up to the energy of the ^{10}Be peak. The rate of such events is very low and it does not interfere with our ^{10}Be measurements.

3.2.5 Gas quality

In the ionization chamber we use isobutane ($CH(CH_3)_3$) as counting gas. There is a permanent flow of isobutane gas from the gas bottle to the ionization chamber and from the ionization chamber to a vacuum pump. The gas pressure is regulated

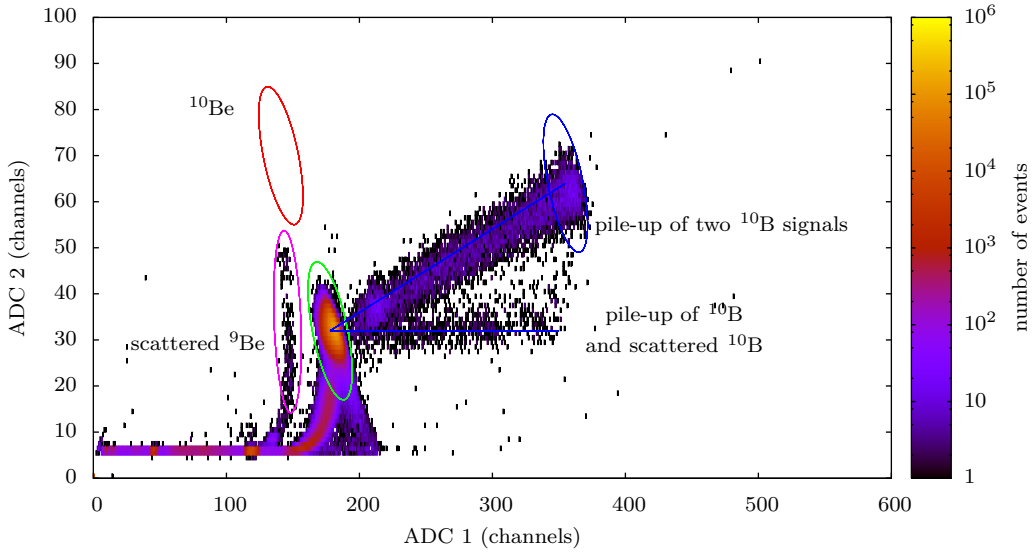

Figure 3.10: The spectrum of a BeO blank sample (Material: Q1p). This spectrum is a sum of all runs on this cathode with a total measurement time of 4391.31 s. The switching magnet had been tuned for $^{10}Be^{4+}$. No ^{10}Be has been counted for this sample cathode. Because of this long measuring time, the spectrum exhibits the ^{9}Be background.

by adjusting the valve that connects the ionization chamber and the vacuum pump. When the ionization chamber is not in use, it is evacuated and a bypass valve to the beam line is open.

Figure 3.12 shows an overlay of early spectra and later spectra of the same measurement. The peaks have shifted to the upper right with time. It is unlikely that both amplifiers had the same drift in gain. A drift in gas density, i.e. a change in gas pressure or temperature, would look differently: the peaks would move to the upper left for lower density and to the lower right for higher density.

The shift of the peak positions was probably caused by an improper gas in the detector at the beginning of the measurement. The gas impurity has reduced the pulse height. Later the gas has been washed by the continuous flow of gas.

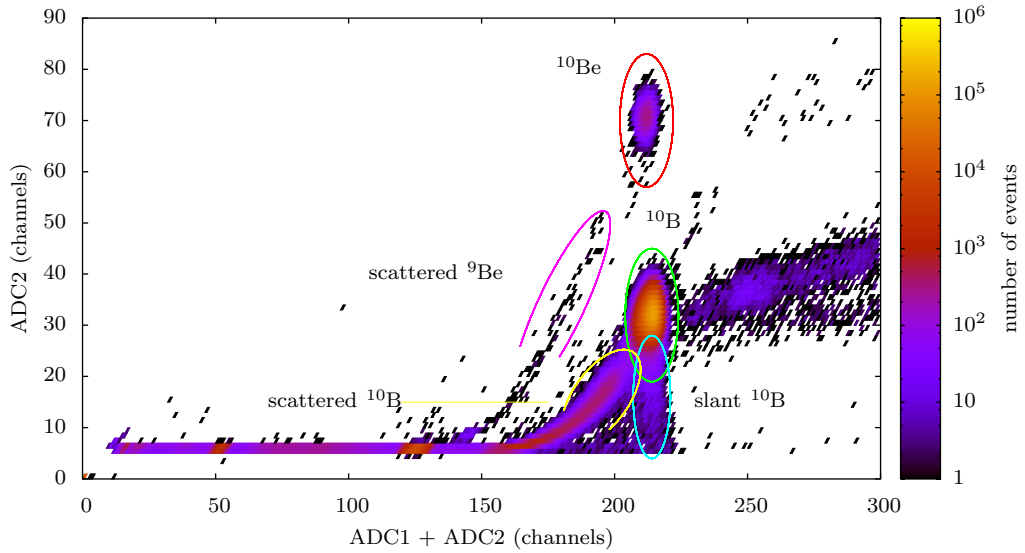

Figure 3.11: This spectrum shows the total energy on the x-axis. (The data is the sum of some spectra from the Be_ng1_poststrip measurement.) The ^{10}B peak has two tails: ^{10}B ions taking a slant path through the detector give a signal with the same total energy but more energy loss in the first section. Scattered ^{10}B on the other hand has lower total energy. The maximum total energy of ^{9}Be is roughly 90 % of the ^{10}Be energy.

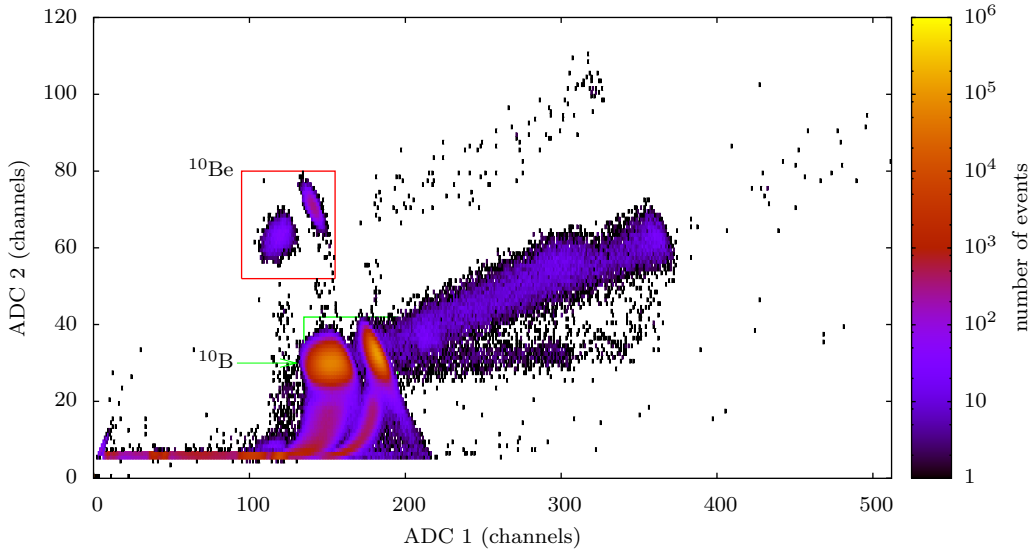

Figure 3.12: This spectrum is the sum of some early runs and some late runs. There was a drift in the peak positions. We account this to gas impurities in the ionization chamber at the beginning of our measurement. For the evaluation I had to set up large bins to include both peak positions.

3.3 The measurement cycle

The isotope ratios are measured by comparison of the ^{10}Be count rate in the detector and the $^{9}Be^{2+}$ current in the offset Faraday-cup, `MFC 04-2`, after the analyzing magnet. Since the two nuclides cannot be injected into the accelerator at the same time, the multi-beam switcher (MBS) fulfills a measurement cycle, a so called machine cycle which is a time span of about 250 ms. Within each machine cycle the MBS switches between 16 different states. Each state is set up to load one of four registers of parameter values for the MBS as well as the electrostatic steerers in front of the accelerator tank—`ESX 02-1` and `ESY 02-1`. (Cf. figure 3.13)

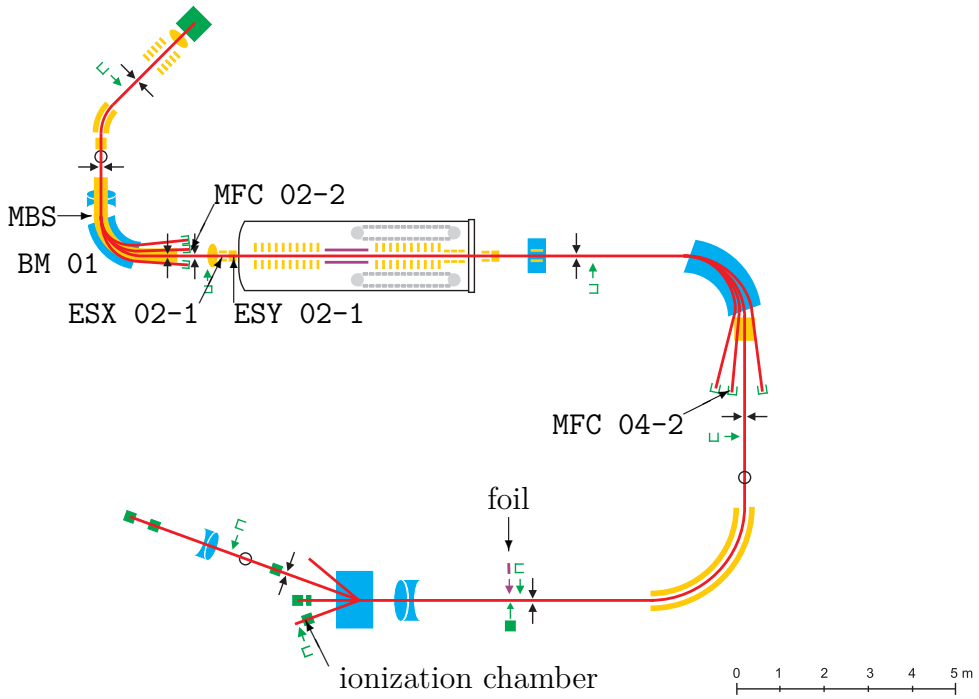

Figure 3.13: Components of VERA for the current measurements

This allows fast switching of the measurement of two nuclides. For the ^{10}Be measurements three registers are used:

`reg0` mass 25 u is injected into the accelerator, this allows the measurement of ^{9}Be in the high-energy offset cup `MFC 04-2`.

reg1 mass 25 u is directed to the low-energy offset cup MFC 02-2. Comparison of the currents in the cups MFC 02-2 and MFC 04-2 allows us to observe the accelerator transmission.

reg3 mass 26 u is injected into the accelerator. The detector counts ^{10}Be. This phase takes up most of the time of a machine cycle, to get as much counting efficiency as possible.

Detection of ^{10}Be is only possible while reg3 is active. When speaking of count rates, it is always the number of counts over this net measurement time.

To convert a current to a count rate, the frequency of ions ν of the charge Q (which is a multiple of e $= 1.6 \cdot 10^{-19}$ As can be calculated simply from the current I:

$$\nu = \frac{I[\mathrm{A}]}{Q[\mathrm{As}]} \tag{3.5}$$

3.4 Tuning procedure

3.4.1 Temporarily tune in to ^{9}Be

Usually, tuning VERA is done in steps of tuning several parameters in sections starting from the ion source and moving on towards the detector. For this procedure the influence of each parameter on a beam current is observed. For trace isotopes the currents are too low to be measured. In some cases a pilot beam can be used, but in the case of ^{10}Be the pilot beam of ^{10}B from a typical sample is too weak to allow measurements of the current.

Therefore I tune VERA for a ^{9}Be beam and set scaled values for some parameters based on the ^{9}Be setup. During the tuning procedure, the source will have to sputter the same cathode for a long time, therefore we use a beryllium blank cathode rather than a ^{10}Be standard cathode for the tuning in order to minimize cross contaminations.

In the intermediate ^{9}Be setup, a ^{9}Be^{16}O^{-} beam is injected into the accelerator and a ^{9}Be^{2+} beam on the high-energy side passes the high-energy magnetic analyzer BM 03-1 and the electrostatic analyzer ESA 04. The beam is then stopped in the Faraday cup FC L4-1, which is between the ESA and the switching magnet BM 04 just in front of the post-stripping foils. In the beginning I used to use the ^{9}Be current up

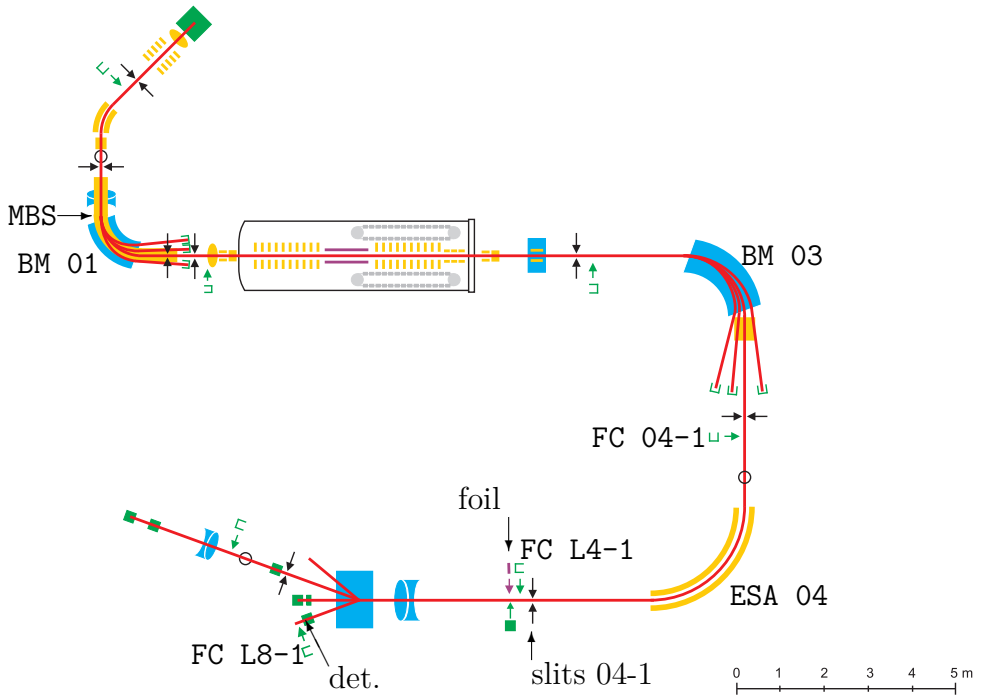

Figure 3.14: Some of the components of VERA involved in the tuning procedure.

to the Faraday-cup `FC L8-1` behind the detector position, passing the slits `Slt L4-1` and the aperture of the detector. Since we have good setups now, I stop ^{9}Be tuning at `FC L4-1`. Anyway, the setup cannot be scaled perfectly to ^{10}Be in this section, because the use of foils needed for post-stripping changes the situation a lot. Tuning with ^{10}B count rate has to be done anyway.

3.4.2 Scaling to ^{10}Be

When the tuning of the intermediate ^{9}Be setup is finished, the setup is scaled in the following way: The injector energy, the low-energy bending magnet and the terminal voltage are chosen to be fixed. Therefore the only parameter on the low-energy side, that has to be scaled is the voltage of the MBS to allow the $^{10}Be^{16}O^{-}$ beam to pass

the low-energy magnetic analyzer, i.e. to keep the magnetic rigidity

$$Br = \sqrt{\frac{2EM}{Q^2}} \tag{3.6}$$

constant. This means that the ion energy has to be lowered by the factor $^{25}/_{26}$ by the MBS. The old value of the MBS can be kept for the `reg0` phase of the machine cycle, when ^{9}Be is to be injected into the accelerator.

Because of different mass, the energy after the molecule breakup will be slightly higher for the ^{10}Be than it is for the ^{9}Be. Therefore, all parameters on the high-energy side have to be scaled. For the `BM 03-1`, the magnetic field has to be scaled in order to keep the same radius of the ions. For the `ESA 04` the electric field has to be scaled with $^{E_{\mathrm{new}}}/_{E_{\mathrm{old}}}$, as we have

$$\mathcal{E}r = \frac{2E}{Q} \tag{3.7}$$

for electrostatic deflectors.

3.4.3 Tuning with ^{10}B count rate

The setup obtained from scaling the ^{9}Be setup will guide a beam with the ion mass of 10 u up to and through the slits `Slt L4-1`. At this point I insert the post-stripping foil and the ionization chamber detector. Starting with the settings from older setups, I now have to find the correct field setting for the switching magnet `BM 04`. This field can roughly be calculated from the expected energy and the chosen charge state. We have done measurements with the 3+ charge state as well as the 4+ charge state.

Fine tuning of the magnetic field can be done by maximizing the total count rate in the detector. Usually, we have to insert an attenuator in the beam in the `S1` section right behind the ion source. It reduces the beam intensity by a factor of ~ 200.

While using the 3 mm aperture in front of the detector, I tune with detector count rate, which is mostly ^{10}B and a negligible number of ^{9}Be counts from the $^{9}\mathrm{Be}^{1}\mathrm{H}^{2+}$ which is broken up at the foil.

3.4.4 Current measurements

By applying the magnet chamber voltage stored in `reg0`, a $^{9}Be^{16}O^{-}$ beam can be injected into the accelerator. This works reliably even after the scaling, because no magnetic components have been changed on the low-energy side. In the high-energy analyzer magnet the ^{9}Be beam will perform the path of an orbit with a smaller radius than for the ^{10}Be. Therefore the ^{9}Be can be measured in an offset cup on the right hand side of the beam line. I use `MFC 04-2` for ^{9}Be. The position for the cup has to be found by scanning its position relative to the beam.

The magnet chamber voltage to be stored in `reg1` can be found by scanning for the current in `MFC 02-2`. This way the $^{9}Be^{16}O^{-}$ current can be measured in `MFC 02-2`. The ratio of the currents in `MFC 04-2` and `MFC 02-2` gives the double of the tank transmission, because the charge state on the high-energy side is 2 and therefore the same rate of ions gives double the current on the high-energy side.

3.4.5 Tuning the switching magnet for ^{10}Be

Now I have an optimized beam of ^{10}B in the detector. Because the stopping power for ^{10}Be is lower than for ^{10}B, ^{10}Be has a higher energy than ^{10}B after the foil. I have to increase the magnetic field of the switching magnet in order to suppress boron and get beryllium instead.

For this, I use a ^{10}Be standard cathode. I increase the magnetic field until the total count rate drops far enough to remove the attenuator and the aperture of the detector and to get about 2000 counts/s, which is just not too high for the data acquisition equipment to cope with. From this point, I start doing measurements with different values of the magnetic field for about 400 measurement cycles—i.e. about 100 seconds—each.

This way I can get the absolute isotope ratios for a number of switching magnet field values. Extensions of the automatic evaluation system of VERA, which I have implemented for the ^{10}Be measurements, are useful for this. A plot and a fit quickly show the optimal field strength with the maximum $^{10}\mathrm{Be}/^{9}\mathrm{Be}$ ratio, which is the point of maximum efficiency.

In some cases at the point of maximum ^{10}Be efficiency the ^{10}B count rate was too high to allow measurements of some samples. However, in most cases, for clean

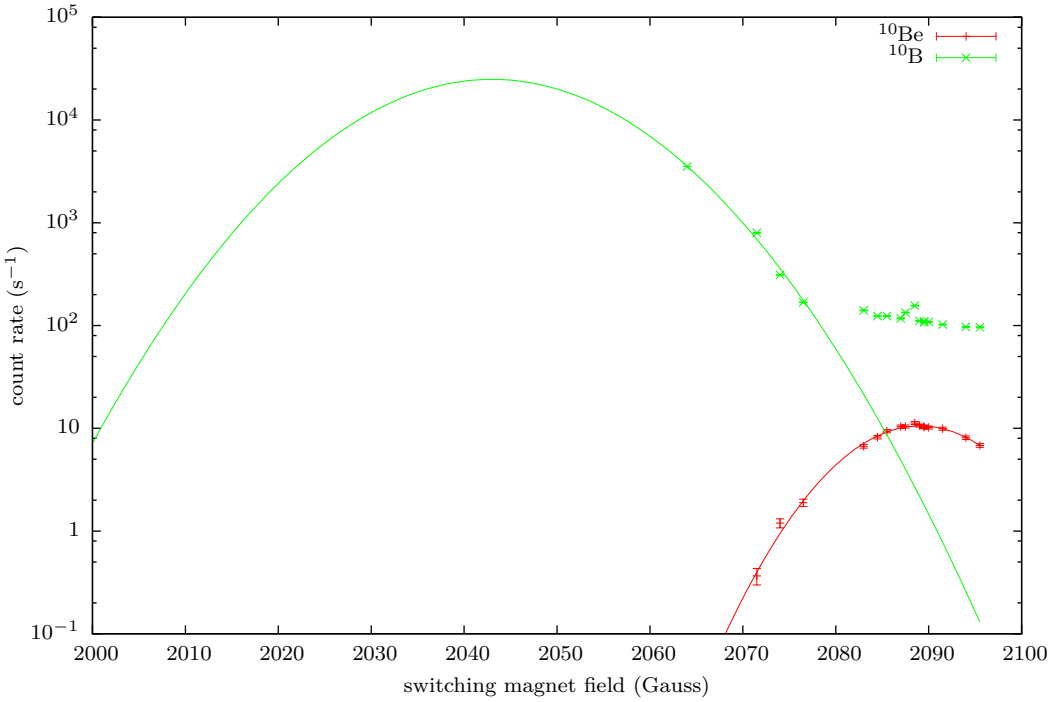

Figure 3.15: A schematic plot of the ^{10}Be and ^{10}B count rates depending on the magnetic field of the switching magnet. The curves are fitted Gaussians. In case of boron the center was fixed as it is known from the tuning process before and only the data up to 2080 G are used.

samples, a 1000 nm foil for the post-stripping has provided sufficient separation. In the case that the count rate is too high, the ion source could be tuned to a lower sputter rate, which gives lower currents and count rates.

I have also tried tuning other parameters than the switching magnet field (namely the steering field in the magnetic quadrupole doublet) for the ^{10}Be count rate, but these attempts have not shown any significant improvement of the efficiency. Therefore I have concluded that it is the best not to change these parameters after the tuning for ^{10}B.

4 Results

The first beam-time in October 2005 revealed that the ionization chamber detector can discriminate ^{10}Be and ^{10}B sufficiently and the post-stripping with a 500 nm silicon nitride foil allows enough suppression of the ^{10}B to reduce the count-rate below 1000 s^{-1}. For the first measurements we selected the 3+ charge state with the switching magnet. Later we changed to the 4+ charge state without much influence on the efficiency, which suggests that both charge states are equally populated.

4.1 Efficiency

The efficiency on the high-energy side, i.e. the ratio of the number of $^{10}Be^{2+}$ ions that pass the high-energy analyzing magnet, to the number of ^{10}Be ions that can be counted in the detector, can be calculated from the ratio of the ^{10}Be count rate in the detector and the $^{9}Be^{2+}$ current in the high-energy offset Faraday-cup for a standard target with known ^{10}Be/^{9}Be ratio. This efficiency is about 7%.

At the beam-time `Be_ng1_poststrip` in June 2006 we noticed that the suppression of boron background is not sufficient for some samples. The count rate became too high. Starting from the next beam-time we used a 1000 nm foil. This reduced the efficiency to about 5%.

measurement	transmission	HE-efficiency	LE-to-detector efficiency
`auer2`	7.2%	72%	5.1%
`Be_ng1_poststrip`	61%	7.0%	4.3%

Table 4.1: Comparison of the efficiencies of the absorber and post-stripping method

The transmission through the accelerator tank was between 50% and 60% thanks to the high stripping yield for the 2+ charge state, compared to 7% for the 3+ charge

state that is used with the absorber method. Thus to compare the efficiency of the two methods we have to use the transmission from the low-energy side up to the detection. This is the product of the tank transmission and the high-energy-side efficiency. Table 4.1 compares two measurements with good efficiency: the beam-time `auer2` in August 2005 using the absorber method and the beam-time `Be_ng1_poststrip` in June 2006 using post-stripping.

4.2 Reproducibility, Accuracy and Precision

In the beginning the results of post-stripping measurements were inconsistent with the measurements of the absorber method. Also multiple standards of the same material in the same measurement had significantly deviating isotope ratios and there was a drift in the measured ratios over the time of the measurement. Figure 4.1 shows the isotope ratios over time for three standards.

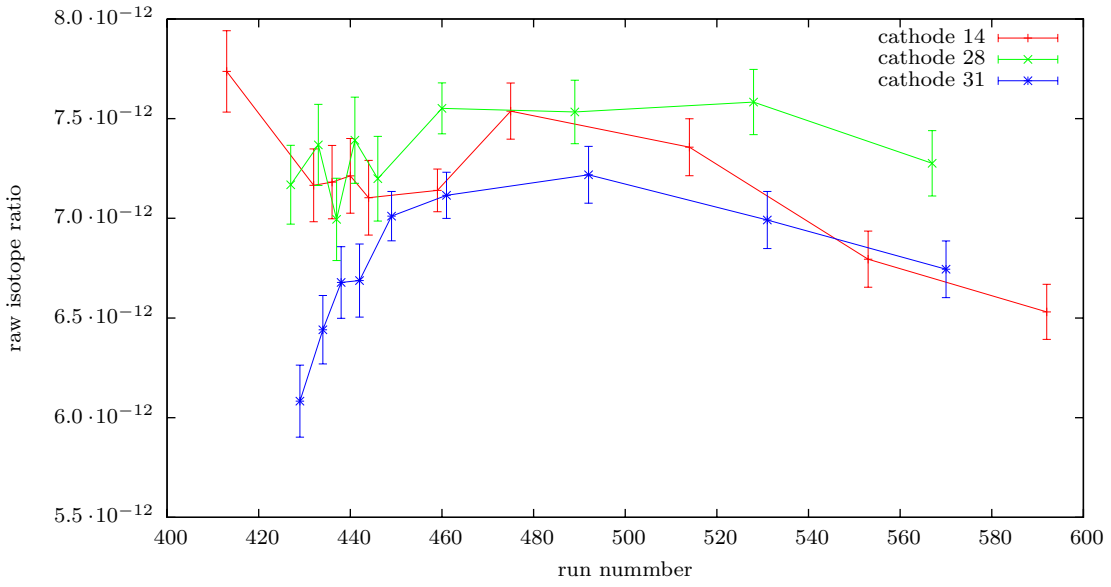

Figure 4.1: Deviations and drift of three standard cathodes in the measurement `poststrip3`. This plot shows the measured raw isotope ratios for three standard cathodes over time. All three cathodes contain the `S555` standard material, which is known to have a $^{10}\mathrm{Be}/^{9}\mathrm{Be}$ isotope ratio of $(9.55 \pm 0.03) \cdot 10^{-11}$. The error bars in this plot show the statistical uncertainty for each run.

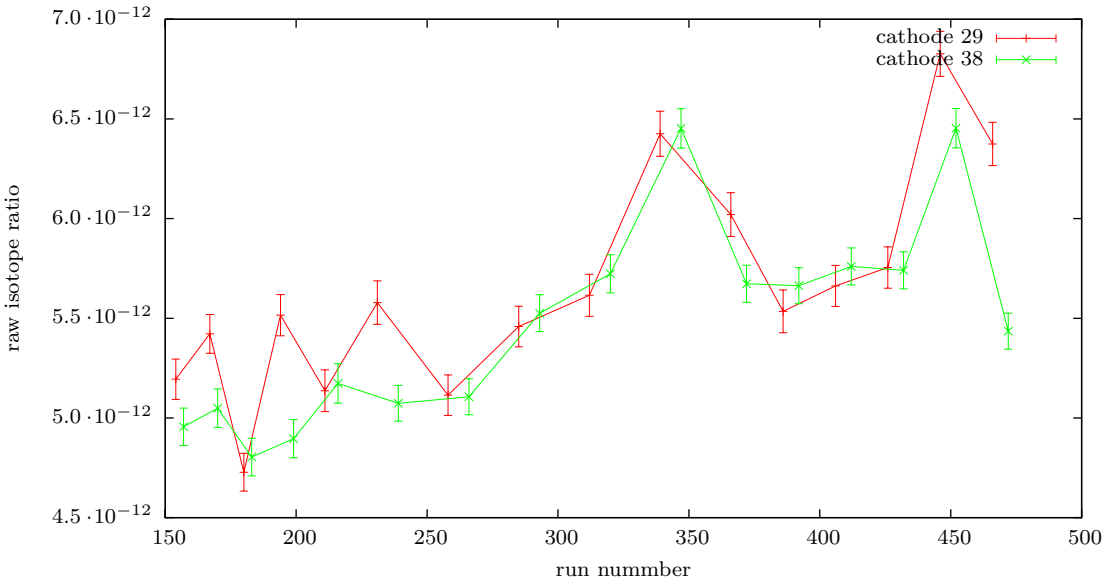

Figure 4.2: Deviations and drift of three standard cathodes in the measurement `auer4`. All three cathodes contain the `S555` standard material, which is known to have a $^{10}\mathrm{Be}/^{9}\mathrm{Be}$ isotope ratio of $(9.55 \pm 0.03) \cdot 10^{-11}$. The error bars in this plot show the statistical uncertainty for each run.

Improvement of the tuning procedure has reduced the deviation problem though there is still drift, see figure 4.2. I have got the notion that the most important point was to make sure to tune the switching magnet to the top of the ^{10}Be peak, rather than maximize the beryllium to boron ratio. Using the 500 nm foil did not allow to do so, because the boron beam was too close to the beryllium beam.

4.3 Boron suppression

Figure 4.3 gives an overview of the efficiency and the boron suppression of a selection of ^{10}Be measurements with post-stripping. The boron suppression is calculated in the following way: in the tuning process, the setup is intermediately tuned for ^{10}B count rate using the attenuator. The attenuation factor can be measured later, by comparing the count rate before and after removing the attenuator. This way I can estimate a $^{10}\mathrm{B}/^{9}\mathrm{Be}$ ratio for the measured sample. With the data from the `poststrip3` beam time I estimate the $^{10}\mathrm{B}/^{9}\mathrm{Be}$ ratio of the `S555` standard material to

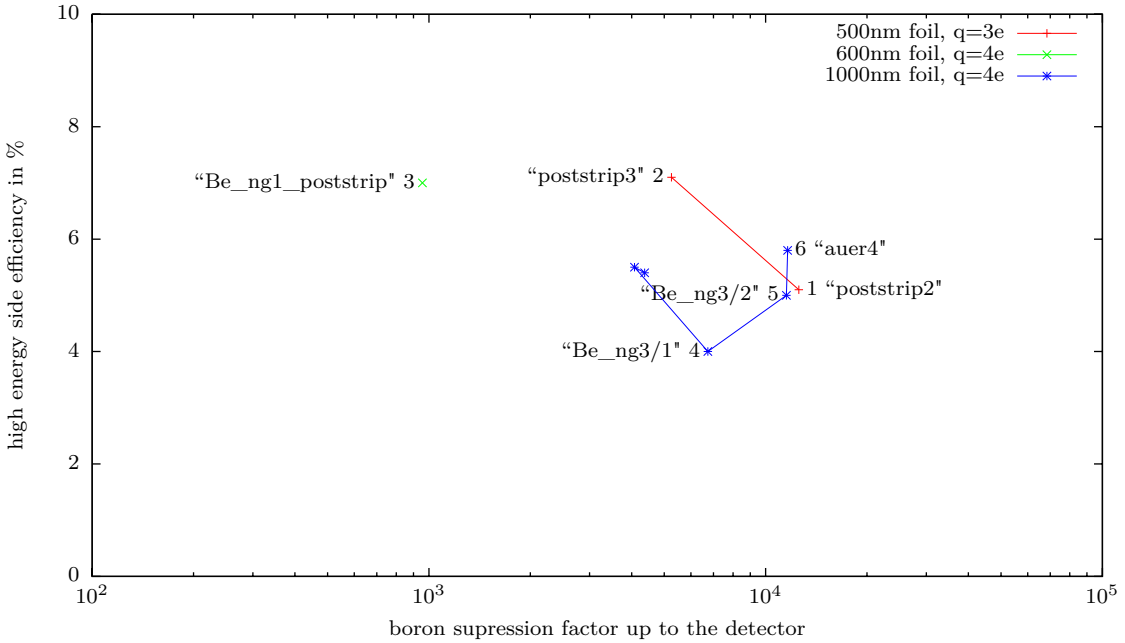

Figure 4.3: High-energy-side efficiency and boron suppression of a number of ^{10}Be measurements with post-stripping. The boron suppression does not include the suppression by the detector itself.

be $7 \cdot 10^{-7}$. This value might well be wrong by up to a factor of 5, because I did not take into account different stripping yield and the different negative ion formation probability for beryllium and boron, but it allows a comparison of the measurements.

The boron suppression of the detector can be estimated from the ratio of boron counts to beryllium counts in a blank sample. For the blank sample material `Bs3` in the measurement `Be_ng3`, this ratio is $3 \cdot 10^6$. Together with the suppression of 10^4 from post-stripping, this gives a total boron suppression of $3 \cdot 10^{10}$ that can be achieved in good tunings.

4.4 Blank measurements

We have measured several blank materials in order to find the measurement background. For the BeO from Alpha Aesar, which we use as spike material, we always measured a ratio in the order of 10^{-14}, when measured with the absorber method as well as with post-stripping. I denote this material as Bα. The measured isotope

ratio for this material is comparable to the finding of Middleton et al. [1984] that commercially available beryllium compounds of some sources contains ^{10}Be at a level of about 10^{-14}.

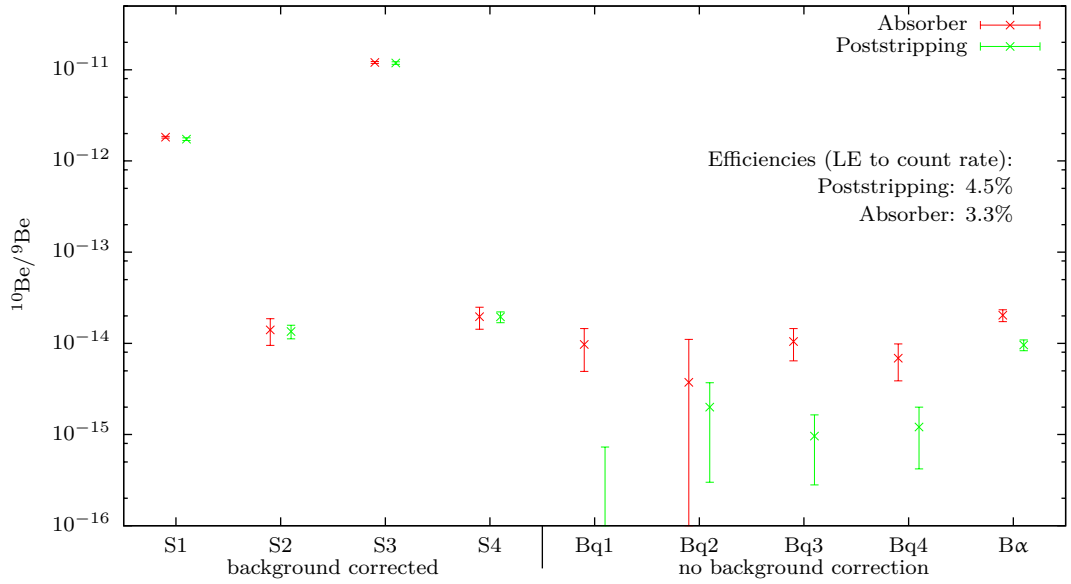

Figure 4.4: Comparison of two measurements of the same sample wheel: `Be_ng1` (absorber method) and `Be_ng1_poststrip` (post-stripping). Materials denoted with S... are ^{10}Be samples, materials denoted with B... are blank materials. The S... samples are spiked with Bα, therefore the Bα ratio can be used for a background correction. Naturally, a background correction cannot be applied this easily to the blank materials.

For other blank materials a lower ratio can be measured and the measured ratio is significantly lower with post-stripping than with the absorber method. Figure 4.4 shows a comparison of the measurements `Be_ng1` and `Be_ng1_poststrip` which were done with the same sample wheel.

Table 4.2 shows the confidence intervals for some recent blank measurements with post-stripping. For these measurements, a standard material with a lower ^{10}Be/^{9}Be ratio was used to reduce the possibility of cross contamination in the ion source.

[1]These values in table 4.2 are not the same as in figure 4.4 because the results of two beam times have been combined. In figure 4.4 I did not do this, because I wanted to compare two measurements done with the same sample wheel.

sample	isotope ratio	confidence interval
Bq1[1]	0	[0 , $6.6 \cdot 10^{-16}$]
Bq2	$2 \cdot 10^{-15}$	[$7 \cdot 10^{-16}$, $4.4 \cdot 10^{-15}$]
Bq3	$9.6 \cdot 10^{-16}$	[$3.4 \cdot 10^{-16}$, $2.1 \cdot 10^{-15}$]
Bq4[1]	$9.5 \cdot 10^{-16}$	[$4.6 \cdot 10^{-16}$, $1.5 \cdot 10^{-15}$]
Bs1	$3 \cdot 10^{-15}$	[$9 \cdot 10^{-16}$, $8 \cdot 10^{-15}$]
Bs2	0	[0 , $1.9 \cdot 10^{-15}$]
Bs3	$8 \cdot 10^{-16}$	[$2.8 \cdot 10^{-16}$, $2.2 \cdot 10^{-15}$]
Bs4	0	[0 , $4 \cdot 10^{-15}$]
Bs5	$2 \cdot 10^{-15}$	[$8 \cdot 10^{-16}$, $4.2 \cdot 10^{-15}$]
all of Bs	$1.3 \cdot 10^{-15}$	[$6 \cdot 10^{-16}$, $2 \cdot 10^{-15}$]
Bα	$1.5 \cdot 10^{-14}$	[$1.3 \cdot 10^{-14}$, $1.8 \cdot 10^{-14}$]

Table 4.2: Confidence intervals for blank samples in the measurements `Be_ng1_poststrip` and `Be_ng3`, which has been performed by Anton Wallner. The Samples `Bq1, Bq2, Bq3, Bq4, Bs1, Bs2, Bs3, Bs4`, and `Bs5` are potential blank materials.

5 Review of the simulations

There is a discrepancy between the ion-optical efficiency from the simulations and from the experimental result. In the simulations the ion-optical efficiency is 51%—i.e. the number of ions entering the detector over the number of ions leaving the post-stripping foil. With a guessed stripping yield of 63% this is a high-energy side efficiency—i.e. ions entering the detector over the number of ions reaching up to the post-stripping foil—of 32%, but only 7% could be achieved in experiments. Table 5.1 shows the stripping yield suggested by the program Q.xls written by Doyle. This stripping yield of 63% is quite low, but even a stripping yield of only 30% would not explain the discrepancy.

charge state	fraction
^{10}Be	$< 1\%$
^{10}Be^{1+}	$< 1\%$
^{10}Be^{2+}	4%
^{10}Be^{3+}	63%
^{10}Be^{4+}	33%

Table 5.1: Result of Q.xls for the charge state distribution for ^{10}Be at 7 MeV.

In this chapter I will try to improve the simulations.

- Experimental data suggests that we underestimated the width of the beam delivered by the accelerator, which I used as initial beam in the simulations.
- A diploma student at VERA, Martin Martschini [in progress], has remeasured the geometry of the beamline section `L4` and the switching magnet and has found errors in the old table of VERA geometry data.
- Comparison of TRIM results and measurements of the energy loss in silicon nitride foils suggest that TRIM gives more accurate results if I assume that the

density of the foils is 2.6 g/cm^3 rather than 3.0 g/cm^3. New TRIM calculations for the changed area density should be used.

Scans of the ^{9}Be current in `FC L4-1` while opening the blinds give a hint about the beam profile delivered by the accelerator. Figure 5.1 shows this scans.

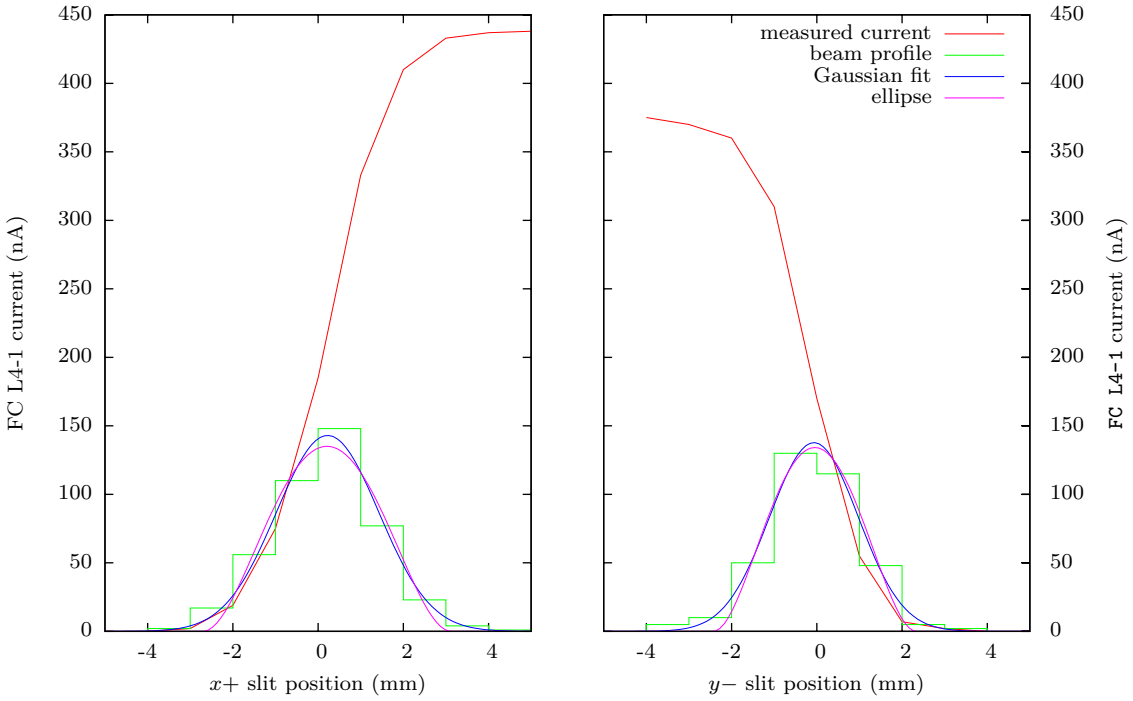

Figure 5.1: Measured beam profile of a ^{9}Be beam at `Slt L4-1`. The left graph shows a scan of the $x+$ slit with open y slits. The right graph shows a scan of the $y-$ slit with the x slits at ± 2 mm. The beam profile is computed as the difference between two adjoining slit positions. Two models are fitted to the profile: a Gaussian beam profile and the profile in equation (5.1). The curve fitting is based on the Levenberg-Marquardt algorithm.

According to Banford [1966] (page 22) the beam profile of a uniformly filled phase-space ellipse is given by equation (5.1)

$$j = j_0 \left(1 - \frac{x^2}{A^2} - \frac{y^2}{B^2}\right)^2 \tag{5.1}$$

where A and B are the half widths of the beam. Figure 5.1 also shows this profile fit to the measured profile. The parameters are $A = 2.9$ and $B = 2.4$.

A Gaussian beam profile fit to the measured profile has a standard deviation of 1.2 mm for x and 1.1 mm for y. Figure 5.1 shows the Gaussian beam profile too.

The Gaussian beam profile fits better to the measured data. Therefore I chose it for new simulations. The beam profile is simulated with a pseudo-random number generator for normally distributed variables using the Box-Muller transform. Figure 5.2 shows a phase-space diagram of this simulated beam. The standard deviation used for x and y is 1.2 mm, and for x' and y' it is 2 mm/m $\approx \tan(2\,\text{mrad})$, which is just a guess.

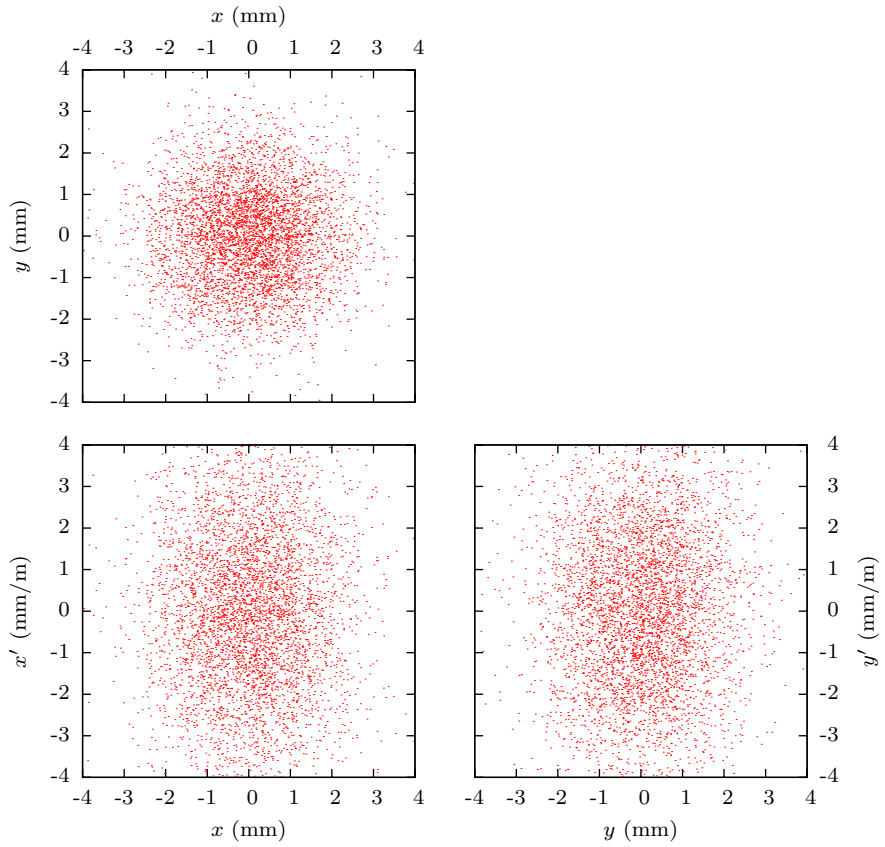

Figure 5.2: Phase-space diagrams of the new simulated beam at the position of `Slt L4-1`. The dots represent the phase-space positions of 5000 simulated ions. The diagrams show three projections of the phase-space slice at the initial position.

Figure 5.3 shows a new simulation that implements all the changes mentioned above. It reflects the setup of the recent measurements, i.e. a 1000 nm foil and the 4+ charge state selected with the switching magnet. Boron can be suppressed completely

in the simulation. The efficiency suggested by this simulation is 5.6%. This is a very realistic value (cf. figure 4.3 on page 60).

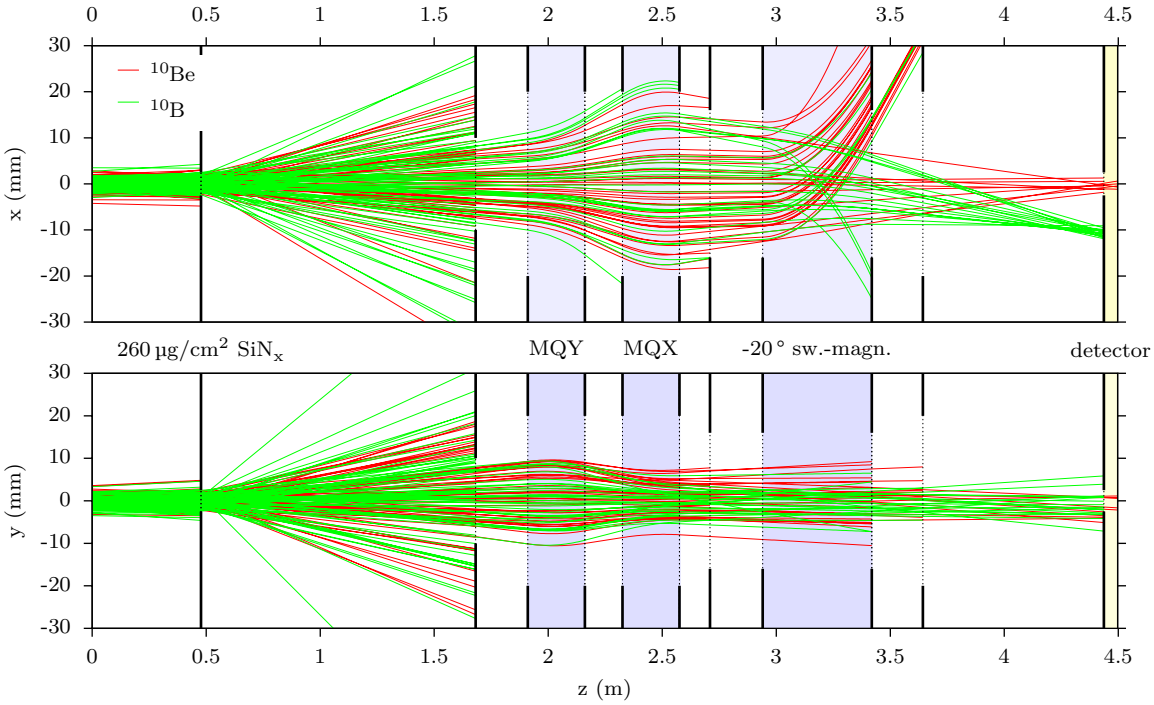

Figure 5.3: A revised simulation of the recent setups using the −20° beam line, a 1000 nm foil and the charge state 4+. The transmission is 5.6%

Although this result is more realistic, it has been adapted a posteriori. The consistency of a single value—i.e. the efficiency—with the experiment, can not provide a significant proof for the accuracy of the multitude of estimated parameters, especially the phase-space distribution of the initial beam. Yet, this revised simulation shows that the discrepancy between prior simulations and the experiment can be explained completely by the uncertainty of parameters in the simulation.

6 Applications of ^{10}Be post-stripping at VERA

6.1 Dating of ice cores

Matthias Auer switched to the new measurement method during his project. He is working on applications of the isotope pair ^{26}Al–^{10}Be in atmospheric and climate research. For this he has investigated variations of the ^{26}Al/^{10}Be ratio in ice and atmospheric samples. He has already presented his work at the 10$^{\text{th}}$ International Conference on Accelerator Mass Spectrometry [Auer et al., 2007]. He will present his results in his PhD thesis [Auer, expected 2007].

6.2 Nucleosynthesis

Post-stripping is not only likely to replace the absorber method for ^{10}Be measurements at VERA. It also introduces new prospects for applications of AMS with ^{10}Be at VERA.

The radiative neutron capture cross sections of various nuclides have an important influence on astrophysical models of nucleosynthesis. Even small cross sections down to a few µbarn are of interest.

One way to measure radiative capture cross sections is by irradiating the reactions target material with neutrons and counting the reaction products with AMS afterwards. For small cross sections, very low isotope ratios have to be measured. Anton Wallner et al. have performed measurements on ^{9}Be(n,γ)^{10}Be cross sections. The ^{10}Be/^{9}Be ratios achieved by neutron irradiation are in the order of only 10^{-14}. This requires, first, blank material with a low ^{10}Be/^{9}Be ratio before irradiation and, second, a

measurement technique with a low background.

The ^{10}Be measurements with post-stripping at VERA promise to provide a measurement technique with a sufficiently low background. Further, the availability of such a technique provides us with the possibility to investigate various potential blank materials for further neutron irradiations [Wallner et al., submitted 2007].

7 Conclusions and outlook

Post-stripping turned out to be a reasonable method for the measurement of ^{10}Be. It is comparable to the absorber method in efficiency and superior in background. Anton Wallner [Wallner et al., submitted 2007] and Matthias Auer [Auer, expected 2007] chose the post-stripping method for their recent ^{10}Be measurements.

Tobias Orlowski, a diploma student, is working on using post-stripping for ^{36}Cl measurements with a silicon strip detector at VERA.

Martin Martschini, a diploma student too, is working on improving the acceptance of the magnetic quadrupole doublet `MQD L4` and the switching magnet. This will probably improve the efficiency.

7.1 Comparison to other labs

Grajcar [2005]; Grajcar et al. [2007] used a similar detector at a 0.6 MV tandem (Tandy) at the ETH Zurich. The efficiency (including the transmission through the high-voltage terminal) was 3-4%, which is comparable to the 4% achieved by us (cf. table 4.1). The background however is 10^{-13}. In Zurich there is also a 6 MV tandem which measures ^{10}Be with an absorber. The background is $5 \cdot 10^{-15}$ [Grajcar, 2005]. The SUERC in Glasgow measures ^{10}Be with a 5 MV tandem and has a background of 10^{-15} in ^{10}Be/^{9}Be [SUERC]. Note that the background measurements were not done with the same sample material. From this comparison it is not clear, if the difference comes from different quality of blank materials or different background suppression.

	Raisbeck et al. [1984]	Grajcar [2005]	this work
terminal voltage	2 MV	0.6 MV	3 MV
overall ^{10}Be transmission	5%	3-4%	4%
background ^{10}Be/^{9}Be	$3 \cdot 10^{-14}$	10^{-13}	$2 \cdot 10^{-15}$

7.2 Further questions

The equilibrium charge state distribution of beryllium stripped with a silicon nitride foil could potentially be measured at VERA for energies up to 15 MeV.

In most of our measurements we used a terminal voltage of 3 MV, partly because one of the Pelletron chains was in bad condition. As these problems are resolved now, I suggest using a higher terminal voltage to improve both stripping yields: in the accelerator terminal and in the post-stripping foil.

Since the beamline at the 40° port of the switching magnet is not used for PIXE anymore, we can finally try the setup that gave the best efficiency in the simulation.

A bigger entrance window for the detector, and slits instead of the round diaphragm could improve the efficiency.

Bibliography

G. Audi and A. Wapstra. The 1995 update to the atomic mass evaluation. *Nuclear Physics A*, 595(4):409–480, December 1995. 13

M. Auer. PhD thesis, Universiät Wien, Fakultät für Physik – Isotopenforschung, expected 2007. 2, 67, 69

M. Auer, W. Kutschera, A. Priller, D. Wagenbach, A. Wallner, and E. M. Wild. Measurement of ^{26}Al for atmospheric and climate research and the potential of ^{26}Al/^{10}Be ratios. *Nuclear Instruments and Methods in Physics Research B*, 259(1): 595–599, Jun 2007. 2, 67

A. Banford. *The Transport of Charged Particle Beams*. Spon, London, first edition edition, 1966. 21, 64

M. Döbeli, C. Kottler, M. Stocker, S. Weinmann, H.-A. Synal, M. Grajcar, and M. Suter. Gas ionization chambers with silicon nitride windows for the detection and identification of low energy ions. *Nuclear Instruments and Methods in Physics Research B*, 219–220:415–419, June 2004. 38

B. L. Doyle. Q. URL `http://www.sandia.gov/pcnsc/docs/q.xls`. 12, 20, 63

O. Forstner, R. Golser, W. Kutschera, L. Michlmayr, A. Priller, P. Steier, and A. Wallner. Potential for the application of compact ionization chambers in AMS at energies below 1 MeV/amu. Poster presented by O. Forstner at the International Nuclear Physics Conference (INPC) 2007, Jun 2007. 38, 39

K. Franzreb, R. C. S. Jr., J. Lörinčik, and P. Williams. Observation of small long-lived diatomic dications BeH^{2+} and BeD^{2+}. *Phys. Rev. A*, 71(2):024701–+, February 2005. 16

R. Golser. Fundamental aspects of ion electron intereactions. In P. Misaelides, editor, *Application of Particle and Laser Beams in Materials Technology*, pages 1–20. Kluwer Academic Publishers, 1995. 17

M. Grajcar. *New concepts of ^{10}Be Accelerator Mass Spectrometry at low energies*. PhD thesis, Swiss Federal Institute of Technology Zurich, 2005. Diss. ETH No. 16249. 4, 16, 38, 69

M. Grajcar, M. Döbeli, P. Kubik, C. Maden, M. Suter, and H. Synal. ^{10}Be measurements with terminal voltages below 1 MV. *Nuclear Instruments and Methods in Physics Research B*, 223–224:190–194, Aug. 2004. 4

M. Grajcar, M. Döbli, P. W. Kubik, H.-A. Synal, L. Wacker, and M. Suter. New concepts of ^{10}Be AMS at low energies. *Nuclear Instruments and Methods in Physics Research B*, 259:173–177, Jun 2007. doi: 10.1016/j.nimb.2007.01.155. 4, 69

D. E. Granger and P. F. Muzikar. Dating sediment burial with in situ-produced cosmogenic nuclides: theory, techniques, and limitations. *Earth and Planetary Science Letters*, 2001. 2

S. Ivy Ochs. *The dating of rock surfaces using in situ produced ^{10}Be, ^{26}Al and ^{36}Cl, with examples from Antarctica and the Swiss Alps.* PhD thesis, Swiss Federal Institute of Technology Zürich, 1996. 2

L. R. Kilius, X.-L. Zhao, A. E. Litherland, and K. H. Purser. Molecular fragment problems in heavy element AMS. *Nuclear Instruments and Methods in Physics Research B*, 123:10–17, 1997. 14

G. F. Knoll. *Radiation detection and measurement.* John Wiley & Sons, New York et al., 1979. ISBN 0-471-49545-X. 44

W. Kutschera, P. Collon, H. Friedmann, R. Golser, P. Hille, W. Rom, P. Steier, S. Tagesen, A. Wallner, E. Wild, and G. Winkler. VERA: A new AMS facility in Vienna. *Nuclear Instruments and Methods in Physics Research B*, 123:47–50, 1997. 4

D. Lal and B. Peters. Cosmic ray produced radioactivity on the earth. In K. Sitte and S. Flügge, editors, *Kosmische Strahlung*, volume 46/2 of *Handbuch der Physik*, pages 551–612. Springer, Berlin, 1967. 1

M. Martschini. Diplomarbeit, Universität Wien, in progress. 63

R. Middleton. A negative-ion cookbook. Unpublished, October 1989. URL `http://tvdg10.phy.bnl.gov/COOKBOOK/`. 7

R. Middleton, J. Klein, L. Brown, and F. Tera. ^{10}Be in commercial beryllium. *Nuclear Instruments and Methods in Physics Research B*, 5(3):511–513, Jul 1984. 61

M. C. Monaghan, S. Krishnaswami, and K. K. Turekian. The global-average production rate of ^{10}Be. *Earth and Planetary Science Letters*, 76:279–287, 1985/86. 1

C. A. Nicolaides, M. Chrysos, and P. Valtazanos. Stability and physicochemical reactions of light dications. *J. Phys. B: At. Mol. Opt. Phys.*, 23(5):791–800, March 1990. 16

A. Priller, T. Brandl, R. Golser, W. Kutschera, S. Puchegger, W. Rom, P. Steier, C. Vockenhuber, A. Wallner, and E. Wild. Extension of the measuring capabilities at VERA. *Nuclear Instruments and Methods in Physics Research B*, 172:100–106, 2000. 4

A. Priller, R. Golser, W. Kutschera, P. Steier, C. Vockenhuber, and S. Winkler. Upgrade of the analysing beam-line at the VERA laboratory. In R. Hellborg, M. Faarinen, C. Magnusson, P. Persson, G. Skog, and K. Stenstrom, editors, *Proceedings of the 35th Symposion of North Eastern Accelerator Personnel (SNEAP)*, pages 68–80, 10 2002. 6

A. Priller, M. Berger, H. W. Gäggeler, E. Gerasopoulos, P. W. Kubik, C. Schnabel, L. Tobler, E.-M. Wild, P. Zanis, and C. Zerefos. Accelerator mass spectrometry of particle-bound ^{10}Be. *Nuclear Instruments and Methods in Physics Research B*, 223:601–607, Aug. 2004. doi: 10.1016/j.nimb.2004.04.111. 2

G. Raisbeck, F. Yiou, D. Bourlès, J. Lestringuez, and D. Deboffle. Measurement of ^{10}Be with a Tandetron accellerator operating at 2 MV. *Nuclear Instruments and Methods in Physics Research B*, 5:175–178, 1984. 4, 17, 69

R. Sayer. Semi-empirical formulas for heavy-ion stripping data. *Reveu de physique appliquée*, 12:1543–1546, Oct. 1977. 20

G. Schiwietz and P. L. Grande. Improved charge-state formulas. *Nuclear Instruments and Methods in Physics Research B*, 175–177:125–131, 2001. 20, 21

K. Shima and T. Mikumo. Equilibirum charge state distributions of ions ($z_1 \geq 4$) after passage through foils: compilation of data after 1972. *Atomic data and nuclear data tables*, 34:357–391, 1986. doi: 10.1016/0092-640X(86)90010-0. 20, 21

P. Steier, R. Golser, W. Kutschera, A. Priller, C. Vockenhuber, and S. Winkler. VERA, an AMS facility for "all" isotopes. *Nuclear Instruments and Methods in Physics Research B*, 223–224:67–71, 2004. 4

P. Steier, R. Golser, V. Liechtenstein, W. Kutschera, A. Priller, C. Vockenhuber, and A. Wallner. Opportunities and limits of AMS with 3-MV tandem accelerators. *Nuclear Instruments and Methods in Physics Research B*, 240:445–451, 2005. 4, 8, 19

SUERC. The suerc accelerator mass spectrometry laboratory, May 2006. URL `http://www.gla.ac.uk/suerc/ams/index.html`. 69

C. Vockenhuber. *The upgrade of VERA for heavy ion AMS and the long-lived radionuclide ^{182}Hf.* PhD thesis, Universität Wien, Februar 2004. 5, 6, 36

A. Wallner, L. Coquard, I. Dillmann, O. Forstner, R. Golser, F. Käppeler, W. Kutschera, A. Mengoni, L. Michlmayr, M. Paul, A. Priller, and P. Steier. Measurement of the stellar cross sections for the reactions ^{9}Be(n,γ)^{14}C via AMS. In *Journal of Physics G: Nuclear and Particle Physics*, submitted 2007. 68, 69

X.-L. Zhao, A. E. Litherland, J. P. Doupé, and W. E. Kieser. The potential for AMS analysis of ^{10}Be using BeF^-. *Nuclear Instruments and Methods in Physics Research B*, 223–224:199–204, 2004. 4

W. Zhou, A. Priller, J. W. Beck, W. Zhengkun, C. Maobai, A. Zhisheng, W. Kutschera, X. Feng, Y. Huagui, and L. Lin. Disentangling geomagnetic and precipitation signals in an 80-kyr Chinese loess record of ^{10}Be. *Radiocarbon*, 49(1):137–158, 2007. 2

J. F. Ziegler and J. P. Biersack. SRIM-2003—the stopping and range of ions in matter. program package, 2003. URL `http://www.srim.org/`. 11, 19, 21, 40

Acknowledgements

Thanks to

Professor Kutschera for leaving this interesting topic to me, for introducing AMS to me, and for many suggestions and corrections to my thesis.

Martin Suter and his team at the ETH Zürich for sharing know-how about ionization chambers with us.

the complete VERA-Team for guidance, help, encouragement, and suggestions for my thesis. Working at VERA was very instructive and pleasurable.

Brian Walsh for proof-reading a draft of this thesis.

I want to thank my parents for their support during my studies. Special thanks to my wife Ayako for her patience, and for persistent encouragement and support.

Curriculum vitae

Name:	**Leonard Michlmayr**
Date of birth:	August 1st, 1978
Place of birth:	Vienna, Austria
Citizenship:	Austria
Marital status:	Married to Ayako Michlmayr née Taniguchi

Schools:

since 2005	*diploma thesis* at the Vienna Environmental Research Accelerator (VERA), Fakultät für Physik – Isotopenforschung, University of Vienna. Advisor: O. Univ.-Prof. Dr. Walter Kutschera
1999–2001	partial study of *Japanese* at the University of Vienna
since 1996	study of *physics at the University of Vienna*
May 1996	*Matura* "mit ausgezeichnetem Erfolg" (school leaving examination)
1988–1996	*Gymnasium* BG Wien XV, Diefenbachgasse 19, Vienna
1984–1988	Volksschule Friesgasse 10, Vienna

Professional experience:

Since 2000 I have worked intermittently part-time for the Schöberl & Pöll OEG and the Leitner-Sidl & Pöll OEG as a computer-network/server administrator.

Publications and Talks:

I presented preliminary results of this work at a symposium of nuclear physics and particle physics in the framework of the annual conference of the Österreichische Physikalische Gesellschaft in September 2006.

A poster on this topic will be presented at the 9$^{\text{th}}$ european conference on accelerators in applied research and technology.

Leonard Michlmayr, Matthias Auer, Oliver Forstner, Alfred Priller, Peter Steier, and Anton Wallner. *AMS measurement of ^{10}Be with post-stripping.* Talk at the 56. Jahrestagung der ÖPG 18.-21.9.2006.

Oliver Forstner, Robin Golser, Walter Kutschera, Leonard Michlmayr, Alfred Priller, Peter Steier, and Anton Wallner. *Potential for the application of compact ionization chambers in AMS at energies below 1 MeV/amu.* Poster presented at the International Nuclear Physics Conference (INPC) 2007.

Anton Wallner, Laurent Coquard, Iris Dillmann, Oliver Forstner, Robin Golser, Franz Käppeler, Walter Kutschera, Alberto Mengoni, Leonard Michlmayr, Michael Paul, Alfred Priller, and Peter Steier. *Measurement of the stellar cross sections for the reactions ^{9}Be(n,γ)^{14}C via AMS.* Submitted to the proceedings of *Nuclear Physics in Astrophysics III*, 2007. Forschungszentrum Dresden-Rossendorf Dresden, Germany.

Lebenslauf

Name: Leonard Michlmayr

Geboren am 1. August 1978

Geboren in Wien

Staatsbürgerschaft: Österreich

Familienstand: verheiratet mit Ayako Michlmayr geb. Taniguchi

Bildung:

seit 2005	*Diplomarbeit* am Vienna Environmental Research Accelerator (VERA), Fakultät für Physik – Isotopenforschung, Universität Wien Betreuer: O. Univ.-Prof. Dr. Walter Kutschera
1999–2001	unabgeschlossenes Studium der *Japanologie* an der Universiät Wien
seit 1996	*Physikstudium* an der Universität Wien
Mai 1996	*Matura* mit ausgezeichnetem Erfolg
1988–1996	*Gymnasium* BG Wien XV, Diefenbachgasse 19, Wien
1984–1988	öffentliche Volksschule Friesgasse 10, Wien

Berufserfahrung:

Seit 2000 war ich mit Unterbrechungen für die Schöberl & Pöll OEG und die Leitner-Sidl & Pöll OEG als Computernetzwerk- und Server-Administrator nebenberuflich tätig.

Veröffentlichungen und Vorträge:

I präsentierte vorläufige Ergebnisse dieser Arbeit im Rahmen der Jahrestagung der Österreichischen Physikalische Gesellschaft September 2006.

Ein Poster zu diesem Thema soll auf der 9$^{\text{th}}$ european conference on accelerators in applied research and technology (ECAART) gezeigt werden.

Leonard Michlmayr, Matthias Auer, Oliver Forstner, Alfred Priller, Peter Steier, and Anton Wallner. *AMS measurement of ^{10}Be with post-stripping.* Vortrag im Rahmen der 56. Jahrestagung der ÖPG 18.-21.9.2006.

Oliver Forstner, Robin Golser, Walter Kutschera, Leonard Michlmayr, Alfred Priller, Peter Steier, and Anton Wallner. *Potential for the application of compact ionization chambers in AMS at energies below 1 MeV/amu.* Poster auf der International Nuclear Physics Conference (INPC) 2007.

Anton Wallner, Laurent Coquard, Iris Dillmann, Oliver Forstner, Robin Golser, Franz Käppeler, Walter Kutschera, Alberto Mengoni, Leonard Michlmayr, Michael Paul, Alfred Priller, and Peter Steier. *Measurement of the stellar cross sections for the reactions ^{9}Be(n,γ)^{14}C via AMS.* Submitted to the proceedings of *Nuclear Physics in Astrophysics III*, 2007. Forschungszentrum Dresden-Rossendorf Dresden, Germany.